



## Article

# CFD Simulation of SCR Systems Using a Mass-Fraction-Based Impingement Model

Max Quissek <sup>\*</sup>, Uladzimir Budziankou, Sebastian Pollak and Thomas Lauer 

Institute of Powertrains and Automotive Technology, TU Wien, Getreidemarkt 9, Object 1, 1060 Vienna, Austria; sebastian.pollak@tuwien.ac.at (S.P.); thomas.lauer@tuwien.ac.at (T.L.)

\* Correspondence: max.quissek@tuwien.ac.at; Tel.: +43-1-58801-31572

**Abstract:** Computational fluid dynamics (CFD) are an essential tool for the development of diesel engine aftertreatment systems using selective catalytic reduction (SCR) to reduce nitrous oxides ( $\text{NO}_x$ ). In urea-based SCR, liquid urea–water solution (UWS) is injected into the hot exhaust gas, where it transforms into gaseous ammonia. This ammonia serves as a reducing agent for  $\text{NO}_x$ . CFD simulations are used to predict the ammonia distribution in the exhaust gas at the catalyst inlet. The goal is to achieve the highest possible uniformity to realize homogeneous  $\text{NO}_x$  reduction across the catalyst cross section. The current work focuses on the interaction of UWS droplets with the hot walls of the exhaust system. This is a crucial part of the preparation of gaseous ammonia from the injected liquid UWS. Following experimental investigations, a new impingement model is described based on the superposition of four basic impingement behaviors, each featuring individual secondary droplet characteristics. The droplet–wall heat transfer, depending on surface temperature and impingement behavior, is also calculated using a newly parameterized model. Applying the presented approach, the cooling of a steel plate from intermittent spray impingement is simulated and compared to measurements. The second validation case is the distribution of ammonia at the catalyst inlet of an automotive SCR system. Both applications show good agreement and demonstrate the quality of the new model.

**Keywords:** SCR; impingement; spray cooling; CFD; ammonia uniformity



**Citation:** Quissek, M.; Budziankou, U.; Pollak, S.; Lauer, T. CFD Simulation of SCR Systems Using a Mass-Fraction-Based Impingement Model. *Fluids* **2023**, *8*, 216. <https://doi.org/10.3390/fluids8080216>

Academic Editors: Markus Klein, Ernesto Benini and Francesco De Vanna

Received: 13 June 2023  
Revised: 20 July 2023  
Accepted: 22 July 2023  
Published: 25 July 2023



**Copyright:** © 2023 by the authors. Licensee MDPI, Basel, Switzerland. This article is an open access article distributed under the terms and conditions of the Creative Commons Attribution (CC BY) license (<https://creativecommons.org/licenses/by/4.0/>).

## 1. Introduction

### 1.1. Motivation

Selective catalytic reduction (SCR) systems are a key technology for diesel engines to reduce the concentration of nitrous oxides ( $\text{NO}_x$ ) in the exhaust gas. While combustion-based methods (e.g., exhaust gas recirculation, air staging) are applied in automotive and industrial applications [1], an additional aftertreatment is necessary for vehicles to comply with increasingly strict emission limits. The preparation and distribution of gaseous ammonia upstream of the SCR catalyst are crucial for an effective and efficient  $\text{NO}_x$  conversion. For the entire catalyst to participate in the reduction process, the ammonia has to be equally distributed across the catalytic brick's cross section. Otherwise, hotspots of over-stoichiometric ammonia concentration may cause ammonia slip, and in particularly lean areas, insufficient  $\text{NO}_x$  conversion can be expected. The transformation from a liquid urea–water solution (UWS) to gaseous ammonia comprises the evaporation of water and the decomposition of urea to ammonia via thermo- and hydrolysis [2]. Part of this preparation is the interaction of UWS droplets with the exhaust system's hot walls and the following vaporization. The impingement process was already shown to be strongly dependent on the droplet's kinetic energy, and the surface temperature [3,4]. As the spray impingement may cause a cooling of the wall [5,6], the impingement behavior of subsequent droplets can, in turn, be influenced. Additionally, the ammonia formation following this evaporation influences the ammonia distribution in the system. Consequently, apart

from generating secondary droplets, the droplet–wall heat transfer must also be captured to predict impingement behavior accurately.

In summary, modeling the impingement behavior and the secondary droplet characteristics, on the one hand, and the associated heat transfer and wall film formation, on the other hand, are crucial aspects of SCR simulation. Observed problems with these two aspects of droplet–wall interaction and possible solutions will be the article’s content.

### 1.2. Impingement Modeling

The first part of modeling droplet–wall interaction describes the droplet’s fate after contact with the wall. The description of this interaction mainly relies on empirical models. Following experimental observations, the outcome of an impingement process is described based on numerous influencing parameters. The main parameters are the surface temperature and the droplet impact kinetics [3,6–8]. Additionally, the influence of surface parameters (e.g., roughness, porosity) or fluid parameters (e.g., viscosity, surface tension) have been reported [9–12].

The influence of the droplet’s impact conditions and its stability is mostly described based on dimensionless numbers, such as Weber-number ( $We$ ) or K-number [3,4,13–15]. The impingement model presented in the current paper is based on an experimental characterization using the  $We$ -number [11]. It is defined in Equation (1) with the wall-normal component of the velocity  $v_n$ , droplet diameter  $d$ , density  $\rho$ , and surface tension  $\sigma$ .

$$We = \frac{\rho v_n^2 d}{\sigma} \quad (1)$$

The temperature influence has been expressed using the absolute surface temperature or a nondimensionalized number  $T^*$  based on surface temperature and liquid saturation temperature [3,4,6,13]. In the current work, absolute values are used.

Good simulation results were achieved in the past, using the established impingement models, e.g., those of Bai and Gosman, or Birkhold [2,3,16] and model extensions [17,18]. However, validation against experimental data revealed shortcomings in certain areas or under specific conditions. The thermal-induced breakup (TBU) behavior was shown to be an essential impingement regime for SCR simulation. Still, it was only described in a first approximation [18]. The necessity for further detailed analysis of this phenomenon (e.g., secondary droplets, temperature boundaries) could be derived from these results. Corresponding experimental investigations were carried out and reported [11,19]. Apart from the further analysis of TBU, experiments indicated a gradual transition between the various impingement regimes instead of step-like changes [11,17,19].

Following the observations, the available impingement models in the literature were analyzed to find a suitable representation of the results. The earlier works, especially, confined themselves to droplet–wall interaction at room temperature and focused on the formulation of a kinetic threshold between film and secondary droplet formation [14,20–23]. Another group of impingement models was designed for elevated temperatures but still below the boiling point of the droplets [24–27]. Some works describe the impingement behavior across a wider temperature range in principle very well, but without detailed information on boundaries or secondary droplets [3,15]. The Bai–Onera model [16] just as the Bai–Gosman model [3] restrict the detailed modeling to the sub-boiling temperature. Research dedicated to higher temperatures focused on the droplet behavior above the Leidenfrost point (LFP) [28]. Naber analyzed secondary droplets of single impingement events at three temperatures (at saturation point, above LFP, and at a transition temperature in between), but no regime boundaries concerning temperature are specified [29].

Kuhnke presents a modeling approach that includes the thermal effect on impingement behavior [4]. Three impingement regimes comprise the model: adhesion (representing film formation), rebound (drop size and wall film remain unchanged), and splash. The splash regime is designed to cover thermal-induced and kinetic-induced secondary atomization. The differences between the two physical effects are described to be represented by

smooth transitions in secondary droplet properties [4]. However, experiments showed a clear difference in physical behavior between the two phenomena [19]. The directions of secondary droplets are different due to the different driving factors, i.e., kinetic energy, on the one hand, and intensive boiling on the other hand. It was observed that, in temperature ranges where mechanical breakup (MBU) and thermal-induced breakup (TBU) coexist, the MBU droplets have very flat ejection angles, and the TBU droplets yield very steep angles [11]. This is in contrast to the described gradual transition of droplet properties for all secondary droplets only with the impact of We-number [4]. Also, no temperature influence on secondary droplets is represented above the deposition limit. The Kuhnke model, therefore, only knows two temperature ranges, one below a dimensionless threshold temperature ( $T^* = 1.1$ ) and one above. The LFP temperature is not represented in the model. Comparable is the model by Senda, which uses the saturation temperature as a threshold [30].

Birkhold’s droplet–wall interaction model is designed to model the impingement of UWS droplets [2]. With the Kuhnke model as a basis, also a single temperature threshold in the regime classification is assumed between a cold and a hot wall. For the application of the model to UWS, this value was changed to  $T^* = 1.19$ . Compared to Kuhnke, two regimes were added: partial rebound and partial breakup. These regimes are designed as a transition with a certain mass fraction assigned to deposition. While these transition regimes are an improvement in modeling the gradual change reported in the experiments, other regime boundaries are still step-like threshold values. In the visualization of spray impingement, a fine aerosol is reported for UWS at 508 K [2]. This is in good agreement with the effect of thermal-induced breakup at this temperature shown in [11]. The reported underestimation of secondary droplets’ spray penetration in the axial direction from the wall in the simulation results could be caused by the missing specific TBU regime in the model. The boundaries of Birkhold’s regime map were confirmed by Börnhorst, but no characteristics of secondary droplets are given [9].

To the best of the authors’ knowledge, no existing impingement model represents the thermal-induced breakup regime as observed and described in previous experimental investigations [11]. Especially the detailed maps about the gradual increase and decrease of TBU influence with changing surface temperature are not yet represented.

### 1.3. Droplet–Wall Heat Transfer

The second important aspect of the droplet–wall interaction is calculating heat transfer during the contact time. Depending on the surface temperature, the boiling behavior, and the energy transfer vary significantly [3,6,31]; see Figure 1.

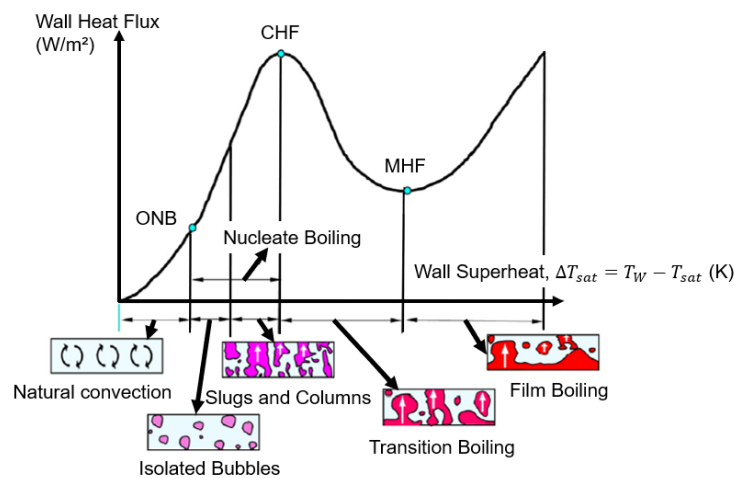


**Figure 1.** Nukiyama pool boiling curve for water at atmospheric pressure. The onset of nucleate boiling (ONB), critical heat flux (CHF), and minimum heat flux (MHF) are plotted. Reprinted with permission from Elsevier [32]; permission conveyed through Copyright Clearance Center, Inc..

Three significant temperatures are essential for the description of the boiling behavior. First, the fluid's saturation temperature  $T_{sat}$ , above which boiling phenomena start to become relevant, and the onset of nucleate boiling (ONB) can be observed. Second, the critical heat flux (CHF) temperature denotes the temperature at which the most vigorous heat transfer between solid and liquid is observed due to the intense formation of vapor bubbles [32]. Third, at the Leidenfrost point (LFP), the vapor film between solid and liquid closes. Consequently, there is no more direct liquid–solid contact and heat transfer is strongly reduced to the minimum heat flux (MHF) by the insulating vapor layer, as shown in Figure 1 [6,32].

Due to this substantial heat flux reduction, the insulation caused by the vapor film is sometimes assumed to be ideal, and the heat transfer above LFP is neglected [3]. However, investigations have shown that, especially for small droplets, this heat transfer is significant [5]. Two phases can be distinguished in this process: a stage of direct liquid–solid contact and another one with reduced heat transfer through a vapor layer [5]. More details are given in Section 2.2.1. In contrast to most impingement models that do not directly cover the heat transfer [3,4,16], a respective modeling approach is discussed and presented in [2]. The proposed model is partly based on investigations by Wruck [5]. For temperatures below the LFP, the Nukiyama approach is used by the author. However, it is stated that the Nukiyama pool boiling correlation is, in the strict sense, only valid for quasi-stationary droplet–wall contact and not for a dynamic impingement scenario [2]. The energy transferred from the wall to the droplet increases the droplet's fluid temperature. In the Wruck heat transfer model, the energy directly evaporates the liquid contact layer of the contacting droplet. Considering the significant influence of heat transfer on the droplet–wall interaction behavior, it seems appropriate to include a heat transfer model directly in the impingement model. Especially at high load points in diesel engines, a temperature in the Leidenfrost range can coincide with high UWS injection mass flows. These conditions can cause significant cooling of the components of the SCR mixing section [33] and, consequently, a sudden increase in film mass in the system when the temperature falls below the LFP. As a possible precursor for deposit formation [34], this phenomenon is crucial in the development of SCR systems. To enable an analysis of the deposition risk, this temperature behavior needs to be captured correctly in the complete temperature range of SCR systems. An established impingement heat transfer model from Wruck was already available. However, experiments showed that the underlying droplet–wall contact changes with the impingement regime. The measured contact time for lower We-numbers allocated to the rebound regime did not match the correlation used by Wruck. The contact area, derived by Wruck from geometrical considerations, can be replaced by well-validated measurement results. A respective adaptation and parameterization of the Wruck approach to UWS and SCR conditions seems a promising approach to obtain an appropriate model.

The scope of the current paper is to present a new impingement model specifically focused on the simulation of urea-based SCR systems. Some experiments that will serve as a basis and part of the resulting data were already presented in [11]. Additional analysis regarding secondary droplets and parameters for a heat transfer calculation is shown in the present report. Finally, with the help of two validation cases, the model's capability will be demonstrated.

## 2. Materials and Methods

Modeling impingement comprises two major parts. On the one hand, the outcome of the impingement event for the droplet must be described, i.e., the formation of a fluid film and the generation of secondary droplets with velocity, direction, and diameter. On the other hand, heat transfer during the droplet–wall interaction is essential. Consequently, in the first section, the distribution of the droplet mass among the impingement regimes is described using a mass-fraction-based classification. The following section deals with heat transfer modeling, while the third part of this chapter describes the resulting secondary droplets. The commercial code Siemens Star-CCM+ v 17.02.008 is used to implement and



test the presented impingement model. However, the general findings and approaches are not limited to a specific code.

The last part will present experiments that serve as validation cases for the developed modeling approach. First, a case demonstrating the heat transfer simulation will be described. Then, the model capabilities to predict ammonia uniformity at the catalyst will be shown for an automotive SCR system.

### 2.1. Mass-Fraction-Based Impingement Modeling

Experimental investigations have shown that the impingement behavior of droplets on hot surfaces can be described using four basic impingement behaviors, shown schematically in Figure 2. Each impingement event either corresponds to one of these regimes or can be described as a mass-fraction-weighted superposition [11].

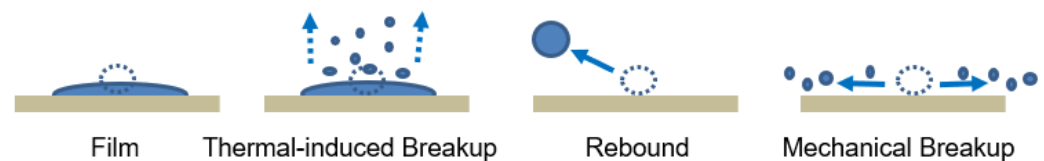


**Figure 2.** Four basic regimes of impingement behavior with characteristic secondary droplets. The dotted circle represents the impinging droplet at the time of first contact with the wall. The arrows show the direction of the secondary droplets [11].

A detailed description of the impingement regimes was given in a recently published paper on experimental investigations [11]. Nonetheless, a short recapitulation will be provided here to facilitate the comprehension of the following modeling approach. After coming into contact with a surface, a droplet may stay attached to form a liquid film (film regime). If the surface temperature is sufficiently high, the film starts to boil almost immediately, and the formation and bursting of vapor bubbles release a fine spray. The secondary droplets generated from this thermal-induced breakup (TBU regime) are ejected from the film almost perpendicular. In case of a rebound, the spread-out droplet retracts again and lifts off the surface like a solid elastic ball (rebound regime). This behavior is enabled by the insulating vapor cushion, which forms between liquid and wall due to very high surface temperatures. With increasing impact energy, the forces spreading the liquid on the surface overcome its cohesive forces, and the droplet disintegrates in a mechanical breakup (MBU regime). The resulting secondary droplets are ejected in all directions from the impact location with a slight elevation angle.

The allocation of droplet mass to the four regimes is based on We-number and surface temperature  $T_w$ . Therefore, when a droplet contacts the wall, the relevant data, e.g., temperatures, diameter, density, velocity, liquid composition from urea and water fraction, and surface tension of the impinging droplet, are extracted and stored. The We-number of the droplet is calculated based on the impingement data.

In CFD simulations of SCR systems, sprays comprising a large number of droplets have to be modeled. A Lagrange parcel approach is used to reduce the numerical effort. This method uses parcels without a numerically resolved diameter, each representing multiple droplets with the same properties (e.g., diameter, density, temperature). The interaction with the surroundings (e.g., drag, gravity, evaporation) is modeled based on these parameters. On the one hand, this reduces the number of droplets to be calculated significantly. On the other hand, it fortifies the demand to correctly represent also mixed impingement behavior, as each parcel represents more mass than a single droplet, thus, increasing its influence on the general result. A set of four impingement maps (e.g., Figure 3) for a given surface roughness is stored in the code as tables. Using the extracted impingement parameters, the relevant mass fraction  $x_{i\_map}$  for each regime  $i$  is then read from the tables. A set of impingement maps for a surface roughness of  $R_z = 7 \mu\text{m}$  is given in Figure 3 [11].

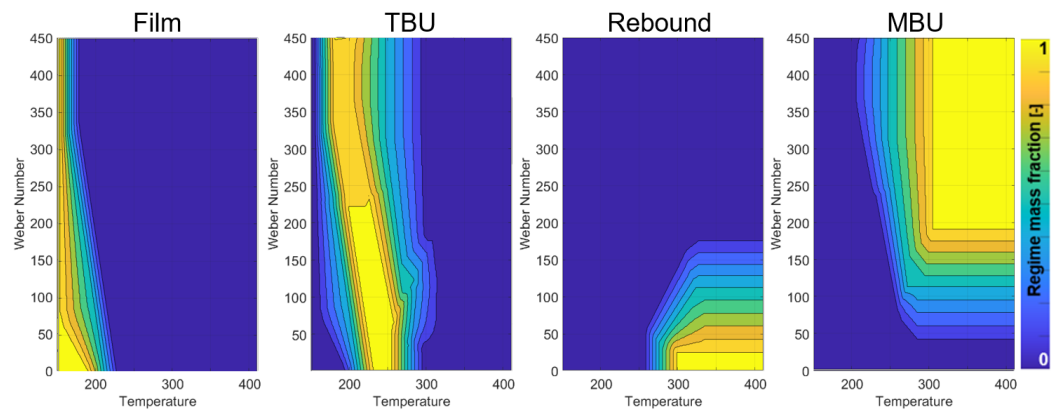


**Figure 3.** Impingement maps for  $R_z = 7 \mu\text{m}$ , showing the mass fractions in the four basic regimes over surface temperature and We-number. (Left): regime film. (Middle left): regime thermal-induced breakup (TBU). (Middle right): regime rebound. (Right): regime mechanical breakup (MBU) [11].

At low temperatures, an impinging droplet forms a wall film. From 150 °C, an increase in temperature causes the film regime to fade out and the mass fraction of TBU to increase (Figure 3: left and middle left). With a further rise in temperature towards 300 °C, the Leidenfrost effect gains influence, reducing the intensity of boiling and TBU (Figure 3: middle left). At high temperatures, rebound and MBU become the dominant regimes (Figure 3: middle right and right). The mass contained in each parcel is divided among those four impingement behaviors according to the mass fractions shown in the plots. For example, at 200 °C and We-number 50, approximately half of the parcel mass belongs to the film regime, while the other half is assigned to the TBU regime.

The given maps represent the interaction between droplets and a dry surface. Consequently, some extensions are necessary in case of impingement on pre-wetted surfaces. Although not studied in detail during earlier experiments [11], observations were made regarding the effect of a wet surface on the rebound probability. A droplet impinging at a sufficiently high temperature with a low We-number typically undergoes rebound. If two droplets hit the exact location within a short time interval, the second impinges on the spread-out first droplet, i.e., a wet wall. In this case, the droplet that would usually rebound undergoes TBU. So no rebound could be observed from wet surfaces, and, consequently, if a wet wall is detected on impingement (film thickness > 1 μm), any mass fraction assigned to the rebound is shifted to the TBU regime instead.

In case a droplet impinges on an already existing thicker film, an additional mass fraction is shifted toward the formation of secondary droplets. This film splash is modeled using a correlation introduced by Bai and Gosman [3]. As the threshold for a minimal film thickness above which the film splash is active, the dimensionless film thickness is implemented as given in Equation (2) with absolute film thickness  $h$  and primary droplet diameter  $d$ . Above a threshold of  $h^* = 0.1$ , film-splash is calculated, i.e., when the film is thicker than 10% of the incoming droplet diameter.

$$h^* = \frac{h}{d} \tag{2}$$

Additionally, the droplet needs sufficient kinetic energy to form secondary droplets and, therefore, has to fulfill the criterion given in Equation (3) [3].

$$We > We_{crit} = 1320 \cdot La^{-0.18} \tag{3}$$

The Laplace-number  $La$  is based on droplet density  $\rho$ , surface tension  $\sigma$ , and dynamic viscosity  $\mu$  according to Equation (4).

$$La = \frac{\rho \cdot \sigma \cdot d}{\mu^2} \tag{4}$$

In case all criteria are met, the film-splash mass fraction  $x_{fs}$  is calculated as in Equation (5).

$$x_{fs} = 0.2 + rand(0.8) \quad (5)$$

In the original formulation, the random share can reach up to 0.9, which, in total, would yield a mass fraction above 1, meaning that an incoming droplet can strike more liquid out of the existing film than its own mass. As the presented impingement model implementation cannot reduce the existing film mass, this random share was reduced to the given 0.8. This way, no more mass can form secondary droplets than impacted with the primary one. This ensures mass conservation. The calculated mass fraction is directly assigned to the MBU regime. The remaining mass of the impinging droplet enters the calculation procedure for dry surfaces.

As a part of the droplet evaporates during contact with the wall, this part of the mass must be deducted before calculating secondary droplets. The calculation of the heat transfer leading to this evaporation will be described in the next section. To deduct the respective mass, the transferred energy has to be translated into a specific mass. Therefore, the enthalpy of vaporization is needed. As described in [2], the enthalpy of vaporization and the reaction enthalpy from urea to ammonia can be combined in a single-step process. This lumped enthalpy is used to calculate the vapor mass fraction  $x_{i\_vapor}$  of the droplet in regime  $i$ . The resulting mass is then deducted from the secondary droplet mass and added to the film fraction. This approach forces the respective liquid mass to form a liquid film on the hot surface. There it boils and evaporates, generating the desired vapor and cooling the surface. The resulting regime mass fractions are defined as given in Equations (6)–(9).

$$x_{film\_final} = [x_{film\_map} (1 - x_{fs})] + \sum x_{i\_vapor} \quad (6)$$

$$x_{rebound\_final} = [x_{rebound\_map} (1 - x_{fs})] (1 - x_{rebound\_vapor}) \quad (7)$$

$$x_{MBU\_final} = [x_{MBU\_map} (1 - x_{fs}) + x_{fs}] (1 - x_{MBU\_vapor}) \quad (8)$$

$$x_{TBU\_final} = [x_{TBU\_map} (1 - x_{fs})] (1 - x_{TBU\_vapor}) \quad (9)$$

## 2.2. Droplet–Wall Heat Transfer

After the regime mass fractions are assessed, the amount of energy transferred between the droplet and the wall during the contact time needs to be calculated. As the authors conducted no direct heat transfer measurements, approaches found in the literature are used as a basis. However, as far as possible, impingement parameters used in the resulting model are taken from or validated with their own experimental data. The authors' data was gathered during impingement investigations reported in [11]. Additional analysis was performed in the scope of the current work to increase the database for modeling. The contact time was evaluated based on high-speed imaging from the first recorded frame with droplet–surface contact to that of fluid–solid separation. The time is then calculated from the number of frames and the frame duration. Regarding the contact area, the maximum length of the contact patch is evaluated. As the images are recorded in side view, only the length of the contact patch is known and not its width. Especially for very flat impingement angles, it can be expected that the form of the contact patch is not circular but elongated. As the width cannot be extracted from the images, a margin of uncertainty remains about the exact contact area between the droplet and the wall.

### 2.2.1. Modeling Approach

Extensive investigations of heat transfer during droplet–wall interaction were performed by Wruck [5]. These insights are especially beneficial as they cover heat exchange under Leidenfrost conditions. Measurements of the contact temperature during impact

on the impingement surface were performed with a very high temporal resolution. A modeling approach is proposed, divided into two heat transfer phases. Figure 4 shows the basic idea with a short phase of direct contact between liquid and solid (Figure 4 (a): ‘ $t_2$ ’, (b): ‘Sudden contact’) with a very steep temperature gradient (Figure 4b: ‘Boiling retardation’). The liquid contact layer is abruptly evaporated from the energy transferred during this direct contact phase and forms a vapor layer between the droplet and the wall (Figure 4 (a): ‘ $t_3$ ’). In the second phase of vapor contact, the surface cools down further until the contact ends with the droplet lifting off (Figure 4 (a): ‘ $t_4$ ’, (b): ‘End of collision’). The reported results show that the smaller the droplet, the more crucial the first direct contact phase is for the overall heat transfer [5].

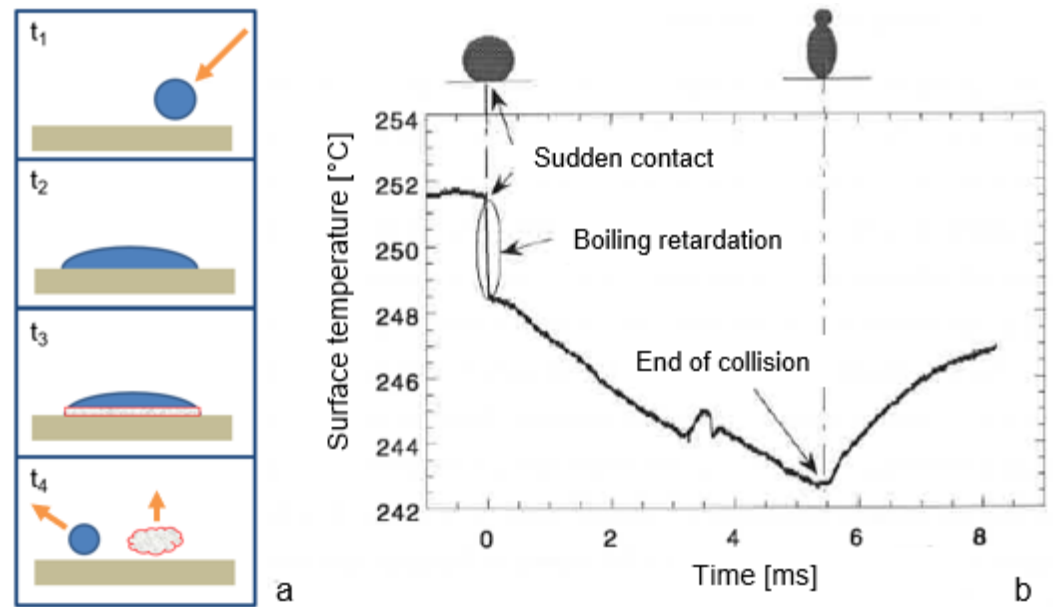


**Figure 4.** Phases of heat transfer during droplet–wall interaction: (a) Schematic of phases. (b) Evolution of contact temperature during impingement (adapted from [5]).

During the direct contact phase, the heat transfer is calculated based on the heat equation and the contact temperature  $T_c$ , as described in detail by Wruck [5] and summarized in the following section starting with Equation (10).

$$T_c = T_w + \frac{b_f}{b_f + b_w} (T_f - T_w) \tag{10}$$

Here,  $T_w$  and  $T_f$  are the temperatures of the wall and the fluid before contact, and  $b_f$  and  $b_w$  are the respective thermal effusivities. The thermal effusivity of a material  $i$  can be calculated based on density  $\rho$ , thermal conductivity  $\lambda$ , and heat capacity  $c$ , using Equation (11).

$$b_i = \sqrt{\lambda_i c_i \rho_i} \tag{11}$$

Finally, with the resulting contact temperature, the heat transfer  $Q_{dc}$  during the direct contact phase is calculated following Equation (12) [5].

$$Q_{dc} = 2A_{dc}\lambda_w(T_w - T_c) \frac{t_{dc}^{0.5}}{(\pi\alpha_w)^{0.5}} \tag{12}$$

Here,  $A_{dc}$  is the contact area between fluid and solid, the thermal diffusivity of the wall material is  $\alpha_w$ , and the duration of direct contact is  $t_{dc}$ . The length of the direct contact  $t_{dc} = 22 \mu\text{s}$  was assessed in [5] experimentally from the duration of the very steep initial gradient of the contact temperature shown in Figure 4b.

Another important finding from these experiments by Wruck regards the calculation of the fluid effusivity from steady-state thermodynamic data as given in Equation (11) [5]. This approach does not yield correct results for the highly overheated liquid resulting from a droplet–wall interaction at high surface temperatures. The liquid effusivity was calculated based on the contact temperature measurements, and the graph in Figure 5 was presented.

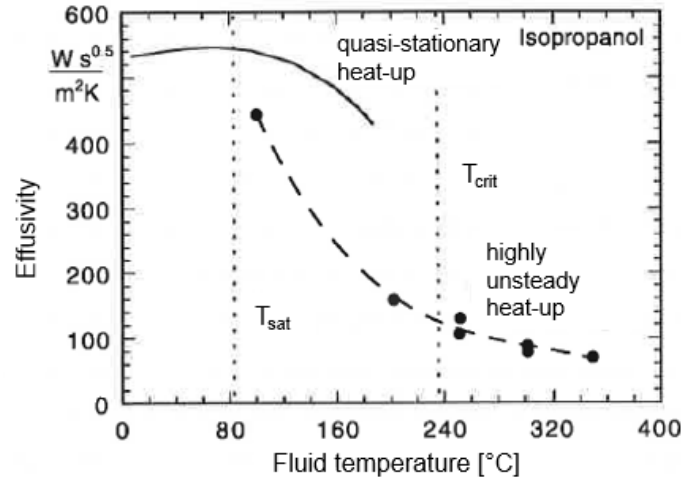


**Figure 5.** Influence of the overheated state of the liquid on the thermal effusivity during the interaction with a hot surface (adapted from [5]).

For the highly unsteady heat-up observed during the droplet–wall interaction, the effusivity is by a factor lower than in the stationary case. The presented data were measured using isopropanol. Unfortunately, no comparable data could be found for other liquids. The stationary effusivity  $b_{UWS_{stat}}$  can be calculated from available UWS fluid properties, Equation (11). On the contrary, the exact behavior in over-heated conditions can only be guessed and leaves a degree of uncertainty. Hence, only a comparable trend was implemented for the unsteady effusivity of UWS. Starting 100 °C above saturation temperature  $T_{sat}$ , a gradual reduction of the stationary value up to a factor of 4 is implemented to determine  $b_{UWS_{unsteady}}$  as shown in Equation (13).

$$b_{UWS_{unsteady}} = \begin{cases} b_{UWS_{stat}} & \text{for } T_f < T_{sat} + 100 \\ b_{UWS_{stat}} \left( 1 - \left( \frac{0.75}{100} \right) (T_f - (T_{sat} + 100)) \right) & \text{for } T_{sat} + 100 < T_f < T_{sat} + 200 \\ 0.25b_{UWS_{stat}} & \text{for } T_{sat} + 200 < T_f \end{cases} \quad (13)$$

In the vapor contact phase, the vapor layer’s thickness influences the heat flux between droplet and wall, and the transferred heat is calculated using Equation (14) [5].

$$Q_{vc} = \int_{t_{dc}}^{t_{vc}} A_{vc} \lambda_v (T_w - T_{sat}) S_v^{-1} dt \quad (14)$$

Here,  $A_{vc}$  is the contact area,  $t_{vc}$  is the end of the vapor contact phase, and  $S_v$  is the vapor film thickness. The vapor contact heat and the direct contact heat yield the total amount of transferred energy.

For the heat transfer calculation, contact area and contact time are necessary. The parameters were analyzed individually for droplet–wall interaction in each regime.

### 2.2.2. Analysis of Droplet–Wall Contact

#### Contact area

The contact area between the droplet and the surface is governed by the influence of the droplet kinetics during impingement. It was shown in several studies [35,36] that for



different liquids and ranges of droplet diameters, the spreading factor of a droplet on the surface can be described based on the We-number as given in Equation (15) [35].

$$\frac{d_{max}}{d_0} = 1 + 0.23We^{0.5} \tag{15}$$

Although the data from the current investigation are limited to the contact patch length  $l_{max}$ , a good correlation with the given formula can be shown in Figure 6 for droplets in the TBU regime. While the data are scattered, the linearization of each data set matches very well with the calculated reference data. The experimental results for the other regimes can be found in the appendix in Figure A1 and are equally well described by the given correlation.

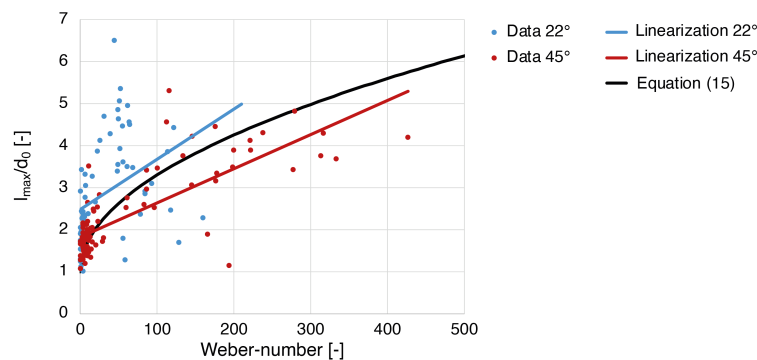


**Figure 6.** Ratio of contact patch length  $l_{max}$  to droplet diameter  $d_0$  over Weber-number. Impingement data from droplets in the TBU regime with 22° and 45° impingement angle and their linearization. The function from Equation (15) [35] is added as a reference.

### Contact time

The contact times between the droplet and the wall differ depending on the impingement regime. According to earlier investigations, the contact time of a droplet during rebound is strongly dependent on droplet size [13,15,37]. It can be described by the Rayleigh time  $t_{Ray}$ , which is derived from the period of a freely oscillating drop and given in Equation (16) [5,6].

$$t_{Ray} = \frac{\pi}{4} \sqrt{\frac{d^3 \rho_l}{\sigma_l}} \tag{16}$$

However, data found in the current study did not show this clear dependence, as seen in Figure 7a. In spite of this, a correlation given below in Equation (17) was applied, which was initially intended for droplets undergoing a breakup, and considers the influence of the We-number. A much better agreement could be found, as shown in Figure 7b. A droplet diameter of 125  $\mu\text{m}$  was used in the calculation to compare experimental data and the given formula. This droplet size corresponds to a Rayleigh time of 150  $\mu\text{s}$  and yields the reference data depicted as a dashed black line in Figure 7b. For an estimation of the influence of the diameter on the comparison, the contact time was also calculated for droplets with 60  $\mu\text{m}$  (Rayleigh time 50  $\mu\text{s}$ , solid black line) and 200  $\mu\text{m}$  (Rayleigh time 300  $\mu\text{s}$ , dotted black line). This range of diameters was chosen as it represents the experimental conditions quite well.

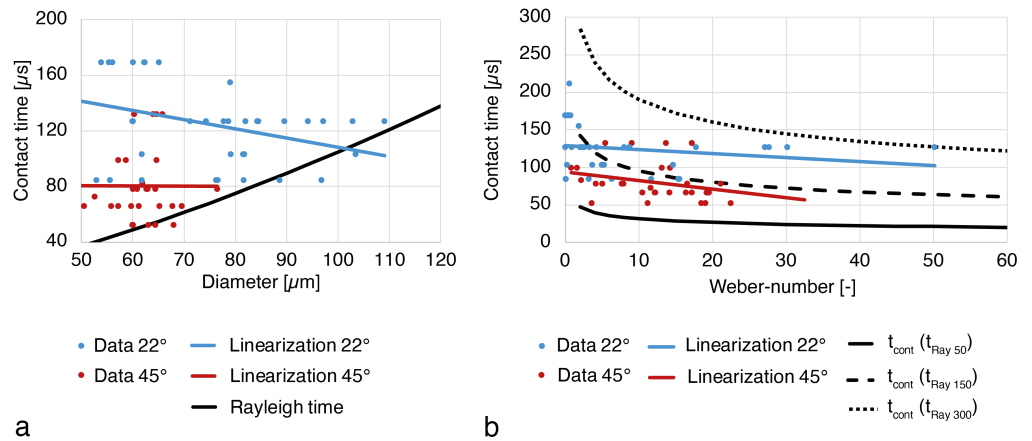


**Figure 7.** Contact time for the rebound regime: (a) As a function of diameter with Rayleigh time (Equation (16)) [5] not matching the measurement data. (b) As a function of We-number with Equation (17) for Rayleigh times 50, 150, and 300 μs [5] and much better agreement.

The contact time in the case of MBU is limited by the ripping of the fluid lamella and, thus, is influenced by the kinetic parameters of the droplet. In the literature [5], a correlation was proposed based on the Rayleigh time but extended by a kinetic factor. This correlation is given in Equation (17).

$$t_{cont_{MBU}} = t_{Ray} \frac{2}{\sqrt{\pi}} We^{-0.25} \tag{17}$$

The plot description for Figure 8a is equivalent to that given for Figure 7b. Droplet diameters and corresponding Rayleigh times are larger to represent better the droplets in the MBU regime: 150 μm with a Rayleigh time of 200 μs (dashed line) and 280 μm with a Rayleigh time 500 μs (dotted line).

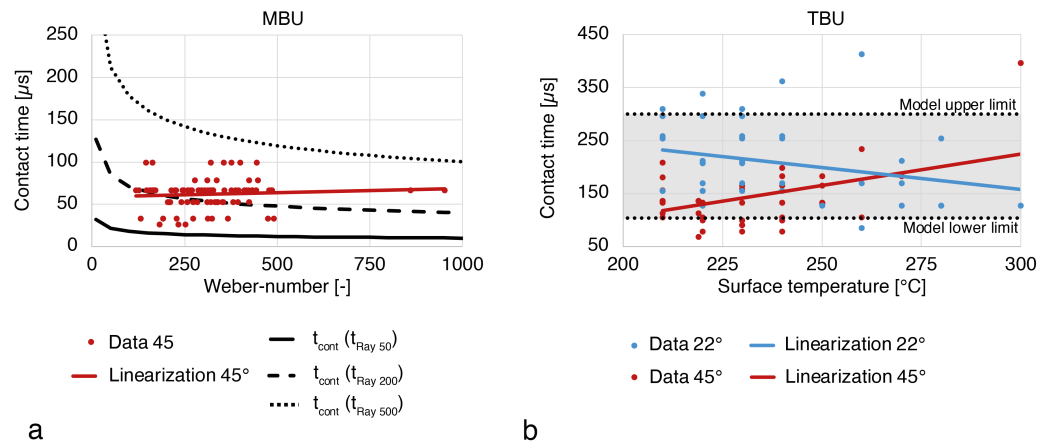


**Figure 8.** Contact time: (a) MBU regime with Equation (17) for Rayleigh times 50, 200 and 500 μs [5]. (b) TBU regime.

As a droplet associated with the TBU regime sticks to the surface, the period of a freely oscillating droplet is not regarded as a characterizing parameter. The boiling behavior and, consequently, the surface temperature are assumed to influence the contact time for these droplets. Hence, the evaluation of contact time is shown based on surface temperature in Figure 8b. No apparent influence of the surface temperature or any significant trend could be identified in the data. However, most evaluated data points could be found between 100 μs and 300 μs. More details on the implementation can be found in the following section.

### 2.2.3. Droplet–Wall Contact Model

**Rebound:** The total contact time for rebound is calculated using Equation (17). As the spreading of the droplet on the surface is a transient process, the contact area changes during the droplet–wall interaction. For a rebounding droplet, the maximum contact area is reached after half of the contact time, as the droplet then starts to retract again. This maximum area is calculated from the droplet diameter and the spreading factor according to Equation (15). As no boundary is given in the literature for this correlation, an upper limit has to be implemented to prevent unrealistically high values. This limit was chosen so that the film thickness resulting from the calculated area cannot fall below 1  $\mu\text{m}$ . From half of the total contact time, when the maximum diameter is reached, the diameter increase per time is calculated. Hence, the contact diameter and area at every given point in time during the spreading phase of the impinging droplet can be calculated.

**MBU:** The contact area in the MBU regime can be calculated similarly, with the only difference being that the maximum diameter is reached at the end of the contact time when the lamella starts to rip apart at its peak diameter.

**TBU:** Following the experimental results, the contact time for TBU is chosen randomly in a range between 100  $\mu\text{s}$  and 300  $\mu\text{s}$ . If the mass fraction of rebound and MBU combined are over 0.9, then the contact time for TBU is shortened. This approach is derived from experimental observations that for high temperatures and small mass fractions of TBU, only very short bursts of secondary TBU droplets appeared. Consequently, also the time for heat transfer must be limited. A possible explanation is the abrupt evaporation of the contact layer during direct contact and the corresponding substantial increase in volume. This expanding vapor was reported in the literature [35] to create a high-velocity vapor flow from beneath the liquid at the rim of the lamella. For very high shares of MBU and rebound, i.e., at temperatures above 300  $^{\circ}\text{C}$ , this vapor expansion is assumed to stop all direct interaction between liquid and wall. Consequently, also TBU ends after the boiling retardation of 22  $\mu\text{s}$ . The contact area for TBU is calculated from the spreading factor and droplet diameter. As the film remains on the surface and the initial spreading phase is short compared to the total contact time, the initial transient phase is neglected, and the peak area is used for calculating the heat transfer.

With these modeled contact parameters, the transferred heat is calculated, and the vaporized mass fraction of the droplet can be obtained.

### 2.3. Secondary Droplet Characteristics

After the regime mass fractions are assessed and reduced by the vapor fraction, the parameters of the resulting secondary droplets need to be calculated.

Crucial parameters of the secondary droplets were evaluated for use in the impingement model during experiments reported in [11]. The data incorporate droplet velocities and directions. As the resulting post-impingement droplets in the experiments are often very deformed, very small, and large in number, the evaluation is prone to a more significant experimental error than in the case of the primary droplets. Otherwise, the droplet detection script follows the same approach described for primary droplets [11]. Droplets from TBU could not all be evaluated individually. Instead, an approximate elevation angle of the ‘spray cone’ of resulting droplets and a range of secondary velocities from a few selected analyzed droplets was assessed. For rebounding droplets, the post-impingement velocities could be evaluated best. The restitution coefficients of pre- and post-impingement velocities in wall-normal and tangential directions were derived from the gathered information. Droplets resulting from MBU could also only be analyzed for some individual cases, gathering information about elevation angles and estimating energy loss during interaction with the wall.

#### Rebound

The post-impact velocities of a rebounding droplet can be characterized by using restitution coefficients, as was shown earlier [3,38]. The correlation proposed in [38] and

given in Equation (18) for the restitution coefficient in the wall-normal direction  $e_{R-n}$  is used as a reference in Figure 9a. A good agreement can be observed.

$$e_{R-n} = 1.0We^{-0.5} \tag{18}$$

While in the literature constant values for the restitution coefficient of the wall-tangential velocity component can be found [3,39], derived from the approach for the wall-normal coefficient, the following correlation is proposed in Equation (19). A good agreement between experimental data and the newly proposed formula for the restitution coefficient in wall-tangential direction  $e_{R-t}$  can be seen in Figure 9b.

$$e_{R-t} = 1 - 1.0We^{-0.5} \tag{19}$$

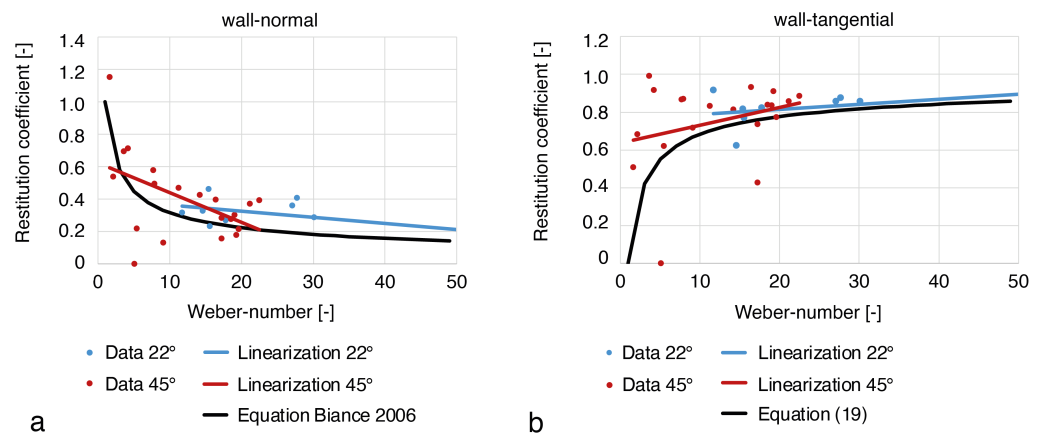


**Figure 9.** Restitution coefficients for a rebound: (a) Wall-normal direction with Equation (18) [38]. (b) Wall-tangential direction with proposed Equation (19).

**MBU**

The direction of secondary droplets from a breakup can be described using azimuthal angles  $\alpha_{azi}$  and elevation angles  $\alpha_{ele}$ . For the elevation angle, a dependency on the We-number is described [40]. A comparison of data gathered in the current experiments and the literature correlation (green) is shown in Figure 10a. While most data points can be found between 0.1 rad (6°) and 0.5 rad (28°), the reported We-number influence could not be confirmed under the current experimental conditions.

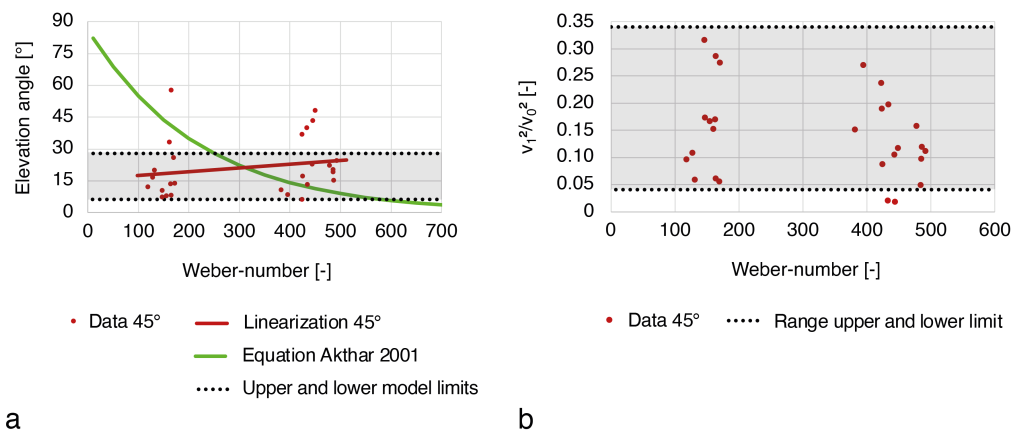


**Figure 10.** Secondary droplet parameters in the MBU regime: (a) Elevation angle with literature proposal from [40] (green). (b) Square of pre- and post-impingement velocity as a measure for energy loss.

The ratio of the squared secondary velocity over the squared primary velocity was analyzed regarding the secondary velocity magnitude after MBU. As shown in Figure 10b, a substantial reduction can be observed. Assuming that the overall mass before and after impingement is constant, the given data would suggest a loss of kinetic energy between 68% and 98%. In reality, a small mass fraction will be lost due to evaporation. As this can be assumed to be in the range of only a few percent, the influence is insignificant in this energy estimation. A part of the energy is not lost but transferred to the increased surface energy of the higher number of tiny droplets with a larger surface-to-volume ratio. Additionally, the secondary droplets are tiny and prone to drag-induced velocity reduction. As the velocity measurement takes a few frames, part of this drag might already be factored into the secondary velocities shown in the graph. Hence, a loss of energy from oscillations and friction between 40% and 70% is assumed. More details on the implementation and the used literature correlations can be found in the following section.

### Secondary Droplet Model Implementation

All secondary droplets need a diameter, velocity components, density, temperature, mass fractions of urea and water, and an injection point within the simulation domain. As Lagrange parcels are used in the modeling, the number of droplets within each parcel must also be defined. The density is assumed to stay constant before and after the impingement. The mass fractions of urea and water are also directly carried over from the primary impinging droplet. The temperature of the secondary droplets is also assumed to match that of the incoming droplet for rebound and MBU, as heat exchange is short and, therefore, limited to the contact layer that uses all energy for evaporation. Only in the case of TBU, the secondary droplets are assumed to be at saturation temperature as they are formed from the thin walls of vapor-filled exploding bubbles. The remaining parameters are calculated individually for each regime as follows.

#### Film

**Diameter:** Film droplets keep their original diameter for the impulse transfer from droplet to fluid film to be calculated correctly.

**Particle count:** To meet the assigned film regime mass fraction of the droplet, the number of droplets in the parcel is reduced accordingly.

**Velocity and direction:** For correct input parameters in calculating momentum transfer to the resulting fluid film, velocity in magnitude and direction are taken over from the primary droplet.

**Injection location:** For every droplet assigned to form film, an injection location is calculated close above the surface. It is found by trailing the path of the primary droplet back a short distance from the impact location to ensure that the injected film droplet impacts within one timestep.

#### TBU

**Diameter:** The diameter of secondary droplets from TBU  $d_{TBU}$  is modeled using a correlation found experimentally by Cossali et al. [8]. It is based on the surface temperature and given in Equation (20). The surface temperature  $T_w$  is in °C, and a lower limit of 1  $\mu\text{m}$  is added for stability reasons.

$$d_{TBU} = d_0 \left( 0.306 - \frac{0.306}{1 + e^{\frac{T_w - 162.5}{11.5}}} \right) \quad (20)$$

**Particle count:** The number of droplets in the particle is calculated to meet the assigned mass fraction of TBU.

**Velocity and direction:** The velocity magnitude is chosen randomly between 0.4 and 8 m/s. This value is mainly driven thermally, presumably by bubble nucleation density, bubble growth rate, evaporation rate, and possibly fluid parameters that influence the thickness and stability of the lamella. Hence, a more detailed calculation would be supposedly numerically costly, and a more thorough investigation was not possible within



the current project. From observations, however, the azimuthal angle of secondary droplets was identified to be randomly distributed around the impact location, and the elevation angle varied randomly between 60° and 90°.

Injection location: The injection location of TBU droplets is the impact location.

Rebound

Diameter: A rebounding droplet is a single droplet. If a part of the mass is lost, its diameter is reduced. Consequently, the diameter is calculated to meet the assigned rebound regime mass fraction.

Particle count: With the mass fraction already considered in the diameter, the number of droplets is kept as in the primary droplet.

Velocity and direction: Looking at the rebound as an elastic interaction between two bodies, the velocity can be calculated using restitution coefficients. This computation is carried out separately for the wall-normal and the tangential direction. The restitution coefficient in the normal direction is calculated using Equation (18). For the restitution coefficient in the tangential direction, the proposed correlation is implemented as given in Equation (19).

Injection location: The injection location is the impingement location.

MBU

In the case of MBU, two secondary Lagrange parcels are created from every impingement event to account for the large variety of possible droplet pathways.

Diameter: The diameter of both droplets is chosen to match half of the mass fraction of the primary droplet assigned to the MBU regime and also considers the increase in particle count due to the breakup.

Particle count: The number of secondary droplets created in the breakup is calculated following an experimentally found correlation [40], which is given in Equation (21).

$$n_{MBUsum} = (0.0427We + 10.46)x_{MBU_{final}} \quad (21)$$

As the correlation was found analyzing We-numbers of up to 750, an upper limit of 50 droplets was implemented to ensure the calculation does not yield exaggerated values for higher We-numbers. With  $x_{MBU_{final}}$ , the mass fraction assigned to MBU and the vaporized portion of the mass are already considered. The particle count is divided among parcel one and parcel two randomly between 30% and 70% each. Finally, for the injection of the parcels, the calculated value is multiplied by the particle count of the primary droplet to meet the conservation of mass.

Velocity and direction: The velocity magnitude of the MBU droplets is found using an energy balance. First, the kinetic and surface energy of the primary droplet is calculated. According to the MBU mass fraction, an equal fraction of the energy is assigned to the MBU droplets and divided equally among the two parcels. Then, using the already available particle counts and diameters, the surface energy of each secondary parcel is calculated and subtracted from the parcel energy. From the remaining part of the energy, a random share of 40% to 70% is assumed to be lost in oscillations and friction, as described in the experimental section. The rest is regarded as the kinetic energy of the parcel. Finally, from the available kinetic energy, the velocity is computed. If there is not enough energy for a positive velocity of the secondary droplets, i.e., if the remaining energy is zero or negative, then the mass is shifted to the film regime to remain on the surface.

Directions of the MBU parcels are defined using azimuthal and elevation angles. The azimuthal angles  $\alpha_{azi}$  take the impingement angle  $\alpha_{ele_0}$  into account and are calculated according to Equation (22).

$$\alpha_{azi} = (-4 + rand(8))\alpha_{ele_0} \quad (22)$$

Defined as such, the MBU droplets can take every direction if their impingement angle is above 45°. For very small impingement angles, the secondary droplets tend to move in the direction of the primary droplet. This implementation represents the observation that

for those sharp angles, a tangential velocity component of the primary droplet is carried over to secondary droplets. The statement is also confirmed by similar reports found in the literature [4].

Following the experimental data, a random distribution between 0.1 radian ( $6^\circ$ ) and 0.5 radian ( $28^\circ$ ) was implemented for the elevation angle  $\alpha_{ele}$ .

Injection location: The injection location for MBU is the impingement location.

## 2.4. Validation Case Surface Cooling

### 2.4.1. Experimental Setup

A holistic approach is necessary to validate the heat transfer properties, as the heat transfer of single droplets was not measured directly. Consequently, surface cooling due to intermittent spray injection over several injection cycles was used as a reference. The experimental results used for comparison were recorded during an earlier project published in [41]. In the exhaust line of a heavy-duty diesel engine, an optically accessible box was integrated. The box has a quadratic cross section of  $200 \times 200$  mm and a length of 600 mm. At the inlet and the outlet of the box, an uncoated monolith is fitted to straighten the airflow through the box and achieve fine-scale isotropic turbulence, as shown in [42]

A model of the box is visible in Figure 11 on the right-hand side. The exhaust gas enters the box from the left and streams along a stainless-steel plate positioned inside the box. On top of the box, an injector is mounted vertically targeting the hot steel plate. Starting from a steady-state temperature, intermittent injection of UWS onto the impingement surface was activated using a constant injection frequency of 1 Hz. The plate's temperature was measured at the black-varnished bottom side through zinc-selenide (ZnSe) windows using infrared (IR) thermography. More details regarding the test bench setup can be found in [41]. The recorded IR images, as shown in Figure 11 at the bottom left, are the experimental reference data. For better orientation, the impingement plate was divided into small sections, named CP3 to CP5. The average temperature values of these areas were recorded, as well as the minimum temperature observed in the impingement areas of the different spray cones. Where specified in a legend, the 'left' spray cone means left in the flow direction, i.e., in the upper right corner of the IR picture. The dark blue areas towards the edges of the images are caused by the steel surface of the box holding the round ZnSe windows. They are only displayed to be colder due to the differing radiation properties.

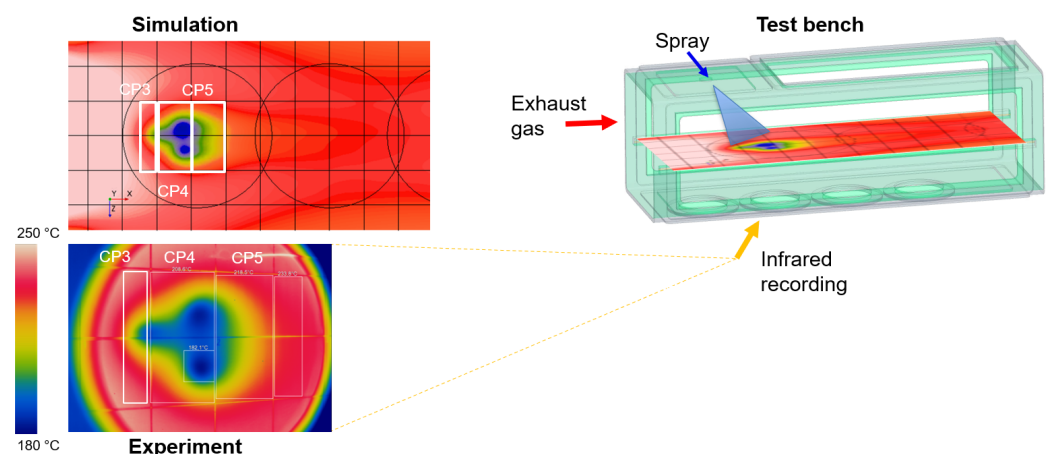


**Figure 11.** The validation test case for surface cooling from spray impingement. Hot exhaust gas flows into a box (**upper right**) to heat an impingement plate exposed to intermittent UWS spray. The surface temperature on the bottom of the plate was recorded with IR thermography (**lower left**) and simulated (**upper left**).

The experiments were conducted with two injectors with different Sauter mean diameter (SMD) values, cone angles, and static mass flows, as detailed in Table 1.

**Table 1.** Parameters of the injectors used in the validation cases [41].

Parameter	Unit	Injector 1	Injector 2
SMD	$\mu\text{m}$	84	178
Static mass flow	kg/h	3.18	7.32
Number of holes	—	3	1
Cone angle	$^\circ$	6	11.5

Additionally, two different operating points of the diesel engine were used to generate the surrounding exhaust gas flow. Consequently, the influence of the gas temperature on the cooling process could be investigated. Engine conditions and corresponding UWS injection parameters are summarized in Table 2.

**Table 2.** Engine and injector operating parameters [41].

Parameter	Unit	Operating Point 2	Operating Point 3
Exhaust gas mass flow	kg/h	1000	1200
Exhaust gas temperature	$^\circ\text{C}$	275	350
Injection mass flow injector 1	mg/s	35.3( $t_{inj} = 40$ ms)	132.5( $t_{inj} = 150$ ms)
Injection mass flow injector 2	mg/s	10.2( $t_{inj} = 5$ ms)	20.3( $t_{inj} = 10$ ms)

#### 2.4.2. Simulation Setup

The whole experimental setup was recreated within the simulation domain using Siemens Star-CCM+ v 17.02.008. A polyhedral mesh with a base size of 2 mm and a total number of 5.2 million cells was used. The boundary layer was resolved with seven prism layers to enable a low- $y^+$ -approach and capture the heat transfer correctly. A mesh sensitivity analysis was performed earlier as reported in [42] to select the appropriate mesh. More details on the mesh, including figures, can be found in [42].

First, the setup was simulated with an inlet cone in front of the first monolith. Here, a mass flow inlet was adopted as a boundary condition. The values for mass flow and temperature can be found in Table 2. At the outlet of the second monolith, a pressure condition is applied with ambient pressure and a temperature of 30  $^\circ\text{C}$ . At the outside of the box, convection is modeled with the ambient temperature and a heat transfer coefficient of 15  $\text{W}/\text{m}^2\text{K}$  [43]. For the radiation heat transfer within and outside of the box, the gray thermal radiation model was adopted together with the surface-to-surface radiation model for calculating the heat exchange within the box [43]. The radiation properties of the materials are given in Table 3. Heat transfer between solid and fluid is modeled with conjugate heat transfer.

**Table 3.** Radiation properties of the surfaces in the box [43].

Surface	Emissivity	Reflectivity	Transmissivity
Impingement plate steel top	0.1	0.9	0
Impingement plate varnished bottom	0.96	0.04	0
Liquid film	0.85	0.15	0
Catalyst	0.9	0.1	0
ZnSe windows	0.13	0.13	0.74
Borosilicate windows	0.9	0.1	0

With this setup, the steady-state flow and temperature conditions were simulated, comparable to the experimental engine tests. These results were used as initial conditions for the following transient simulation with intermittent UWS injection. The cone was removed to reduce the mesh size and save numerical cost. The recorded temperature and velocity field in front of the first monolith was applied as an inlet condition.

The simulation setup for modeling the physical processes in an SCR system is based on the work by Fischer [44]. The turbulent gas flow is modeled with Reynolds-averaged Navier–Stokes (RANS) equations. The V2F  $k$ - $\epsilon$  turbulence-model [45,46] is used with an all  $y^+$  treatment. Additionally to the equations for turbulent kinetic energy and turbulent dissipation, the V2F model solves transport equations for the wall-normal stress component and the elliptic relaxation parameter. This improves the prediction of heat transfer in the boundary layers [45,46]. The injected droplet size distribution was defined using a cumulative distribution function measured with laser diffraction analysis [34]. The droplet–wall interaction, including heat transfer, is simulated using the presented modeling approach. For simulation of the spray propagation, the Schiller–Naumann drag coefficient with Cunningham correction factor was adopted [34]. A liquid film model, including the surface tension effect, was selected to simulate film propagation. Evaporation and boiling were considered as well, based on a Nukiyama boiling correlation.

As a validation, the temperature–time diagram for several areas of the impingement plate is compared between simulation and experimental data, as well as the size and outline of the cooled-down area.

## 2.5. Validation Case Ammonia Uniformity SCR System

The homogeneous distribution of gaseous ammonia at the inlet of the SCR catalyst is crucial for efficient system performance. The ammonia uniformity index (UI) can be used to quantify this homogeneity and, thus, is an indicator for the quality of the ammonia mixing. It is defined as given in Equation (23) with the local concentration  $c_i$ , evaluated area  $A_i$ , the total area  $A$ , and the average concentration  $\bar{c}$  [47]. A value of one shows a perfectly homogeneous distribution.

$$UI = 1 - \frac{\sum_{i=1}^N A_i |c_i - \bar{c}|}{2A\bar{c}} \quad (23)$$

### 2.5.1. Experimental Setup

In earlier experimental investigations, the ammonia uniformity of a heavy-duty SCR system was analyzed on an engine test bench [42]. The mixing section and the catalyst are shown in Figure 12.

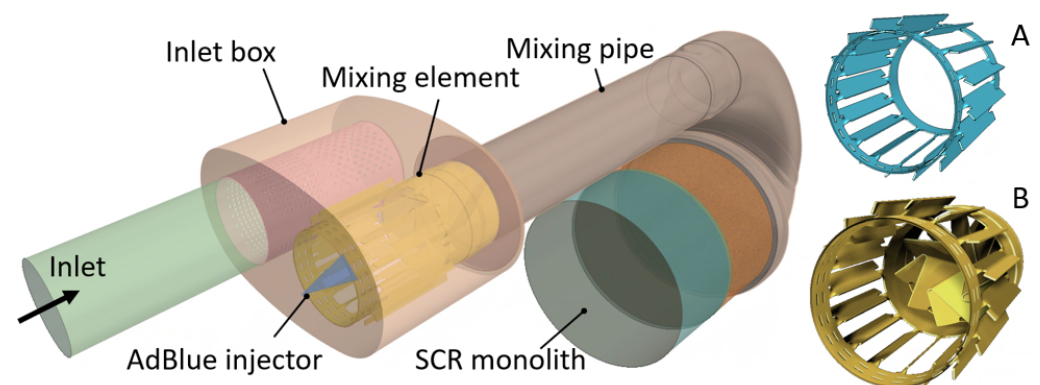


**Figure 12.** Geometry of the SCR system with swirl element A and additional mixing element B.

The ammonia distribution across the outlet of the catalytic brick was measured on the engine test bench using chemoluminescence detection (CLD). More details on the measurement procedure can be found in [18]. The investigation was performed at an

exhaust gas mass flow of 900 kg/h and a temperature of 425 °C. A single cone injector with a spray angle of 48° was used with a measured SMD of 57.8 μm. The UWS injection rate was 694 mg/s with an injection frequency of 1 Hz. This high-load engine operating point was chosen to assess the impingement model quality, as previous results were considered unsatisfactory.

The exhaust system was analyzed with and without an additional swirl mixing element installed in the mixing section, as shown in Figure 12. This extra part is also a primary impingement surface for the spray. Consequently, impingement behavior is regarded as a crucial influencing factor.

### 2.5.2. Simulation Setup

The mesh consists of 7.7 million polyhedral cells with a base size of 4 mm and is depicted in Figure 13. The boundary layer is resolved with eleven prism layers to enable a low  $y^+$  approach. Pipes and mixing elements are modeled as solid parts. The cells for the catalyst are extruded from its inlet and treated as a porous medium.

At the inlet of the exhaust system, a mass flow boundary condition is applied with the mass flow from the engine test bench of 900 kg/h and an exhaust gas temperature of 425 °C. At the outlet of the catalyst, a pressure outlet boundary is applied with ambient pressure and a temperature of 30 °C. As the exhaust system on the test bench was very well insulated, the outside of the system components is modeled as adiabatic. The UWS spray is initialized using a tabled cumulative distribution function (CDF) for the droplet size and the measured values for injection mass flow, spray opening angle, and initial droplet velocity.

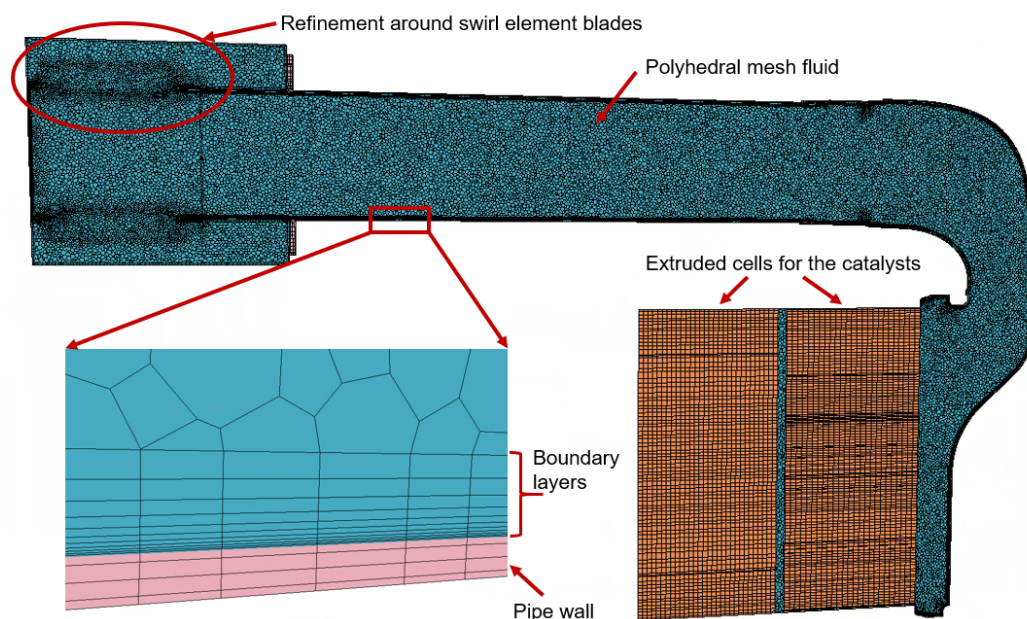


**Figure 13.** Polyhedral mesh of the SCR system (inlet box, mixing pipe, and catalyst) with refinements around the swirl blades, extruded cells in the catalyst (orange), and the boundary layers in detail (fluid in blue, solid in rose).

The simulation setup is, in principle, the same as described for the first validation case above. The most significant difference is the turbulence model. As the presented exhaust system has a relatively complex flow field (swirl flow in combination with a 180° pipe bend), the lag elliptic blending  $k-\epsilon$  model is used [46,48]. It is recommended for complex flow cases with streamline curvature and rotation, as it takes the influence of a misalignment of the principal axes of the strain rate and the anisotropy tensor on the turbulent kinetic energy production into account [46,48]. Further, it had been successfully applied to the current geometry previously [42]. The second alteration is eliminating the radiation heat



transfer model to save numerical effort. This is enabled by the already-mentioned excellent thermal insulation on the test bench.

Apart from the flow field, impingement is a main influencing factor for ammonia uniformity. Consequently, a high-quality impingement model is crucial for a correct uniformity prediction. CFD simulations using a standard impingement model (Bai–Gosman) underestimated the UI for both mixer geometries. The operating temperature of 425 °C is above the LFP and, therefore, most impingement models assume no evaporation during droplet–wall contact. This seems to cause an overestimation of droplet mass reaching the catalyst in liquid form. The consequence of its evaporation on the catalytic brick is an increased intensity of ammonia-rich areas. Especially for the mixer geometry B, which shows an excellent distribution on the test bench, the error in the simulation result is significant. In this geometry, the interaction between spray and mixer is more intense, so the effect of droplet–wall interaction and its modeling is more dominant. Thus, the presented simulation case is an essential test for the validity of the proposed modeling approach.

### 3. Results and Discussion

The capabilities of the droplet impingement model for simulation of the interaction between UWS droplets and hot surfaces will be shown using the two validation cases. First, the surface cooling from intermittent spray injection is shown. Second, the ammonia distribution at the cross section of the catalyst of an automotive SCR system is simulated.

#### 3.1. Validation Surface Cooling

The plate's temperature at the beginning of injection was simulated in a steady-state simulation. The temperature distribution could be well-replicated with a maximum deviation between experimental and simulation data in the worst point of 1.6 °C (case 1), 1.1 °C (case 2), and 3.1 °C (case 3).

Case 1: operating point 2/injector 1

The distribution and location of the cooled-down area could be replicated very well, as is visible in the plots in Figure 14. The agreement of the absolute temperature drop in simulation and experiment is also acceptable for most parts of the temperature–time diagram, especially the gradient during the first 30 s. For the second half of the experiment, the simulated temperature drop underestimates the experimental values slightly. Possibly, this is because the evaporation in the simulation is slightly retarded as the evaporating mass has to be injected onto the surface first. In reality, it evaporates instantly, as shown in [5]. Consequently, film thickness might be overestimated somewhat, causing the influence of the film splash to gain traction at some degrees Celsius higher than in reality. After 77 s the minimum temperature is 185.5 °C in the simulation case compared to 175.8 °C in the experiment.

Case 2: operating point 2/injector 2

Using injector 2 with a single hole and larger SMD, again, an excellent agreement for the cooled area and location can be achieved. Figure 15 shows how the initial gradient of the temperature is also captured well. In this case, however, the value at which the cooling eases off to reach a steady value is lower than expected from experiments. The threshold value for minimal film thickness, above which film splash is active, is a ratio to the droplet diameter. Consequently, for the larger SMD of injector 2, the threshold thickness tends to be larger than for the smaller SMD of injector 1. Hence, an influence can be expected only above a larger film thickness that might take longer to build up. Possibly, the correlation for the film splash threshold needs more thorough investigation in the future. After 57 s of injection, the resulting minimum temperature is 188.5 °C compared to 201.0 °C, yielding an error of 12.5 °C.

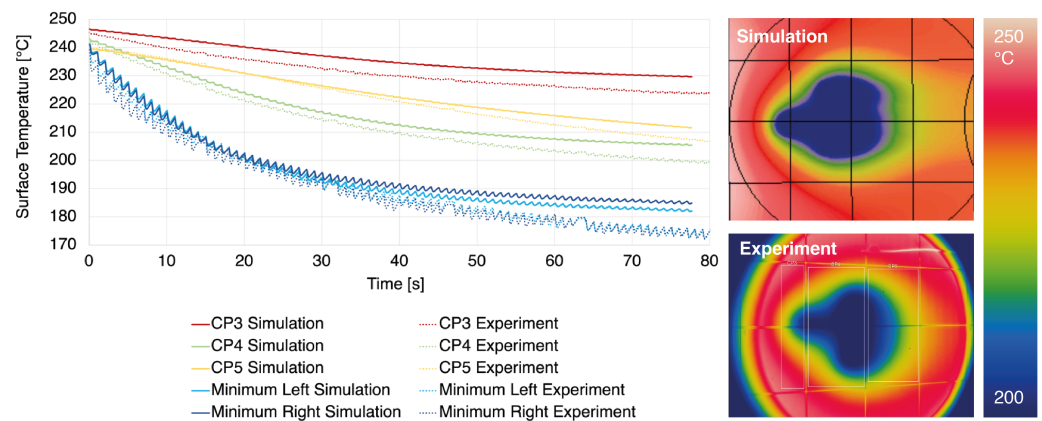


**Figure 14.** Temperature–time diagram of the surface cooling at engine operating point 2 with injector 1 and resulting cooled areas in simulation and experiment after 60 s.

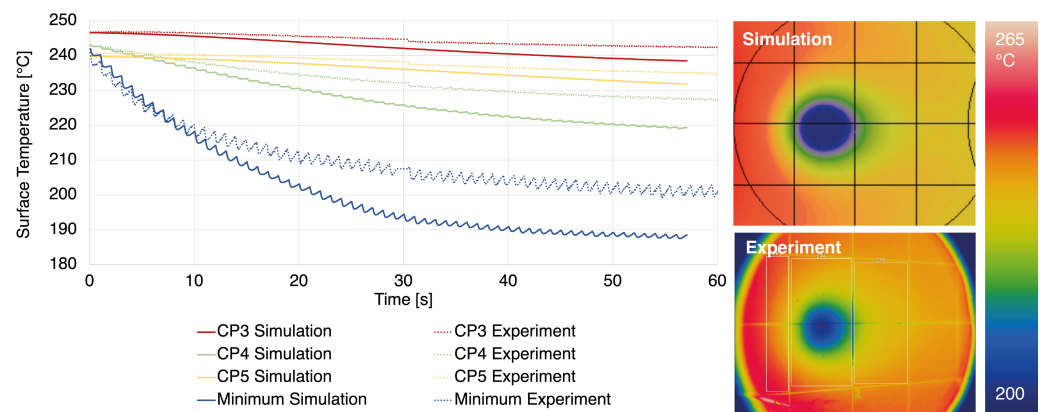
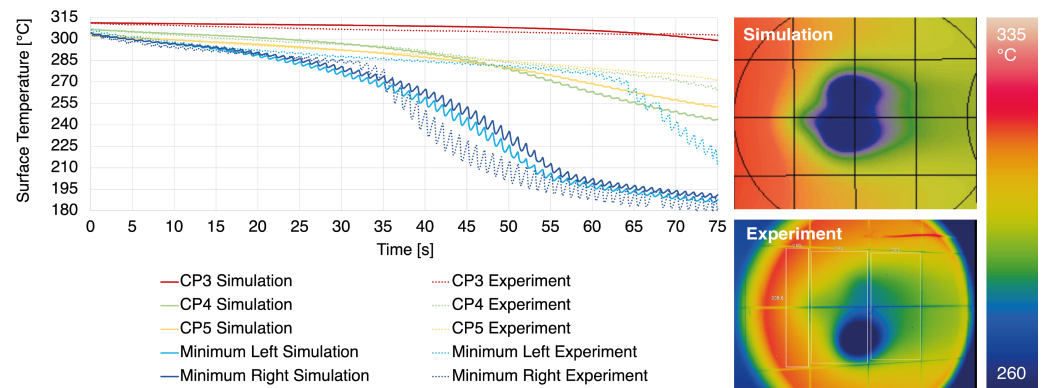


**Figure 15.** Temperature–time diagram of the surface cooling at engine operating point 2 with injector 2 and resulting cooled areas in simulation and experiment after 50 s.

**Case 3: operating point 3/injector 1**

The last presented case depicted in Figure 16 is an example of the operating point 3 with a starting temperature of the surface above 300 °C. Here, the much slower cooling at the high-temperature regimes MBU and rebound at the beginning compared to the cooling effect from TBU can be observed. The resulting flat temperature gradient during the first 25 s is predicted accurately. A peculiarity of this experimental data set is the substantial deviation between the cooling from the left and the right-hand side injector spray cone. The plot shows that the shift from slow to fast cooling occurs much earlier in the right impingement area than on the other side. A more detailed analysis of the injector during the investigations in [34] revealed a difference in mass flow through the individual injector holes. Although this mass flow difference was considered in the modeling process, the strong influence could not be reproduced. Apart from the mass flow, other injector parameters may have been altered for the respective injector hole, e.g., the SMD, due to a partial blockage of the orifice. However, these parameters were not investigated at the time, and more detailed data on the injector are unavailable. A possible influence can only be assumed but not represented in the simulation model. Although not as abrupt as in the recordings, the shift from the slow cooling at high temperatures to the steeper temperature gradient from TBU could be replicated in the simulation. Finally, the transition from fast back to slower cooling also agrees well with the experimental data. 75 s after the start of injection, the temperature minimum in the left spray cone (light blue) in the experiment is 212.5 °C and in the simulation 191.1 °C. However, the relatively large error of 21.4 °C is primarily caused by the later cool-down in the experiment. For the impingement area

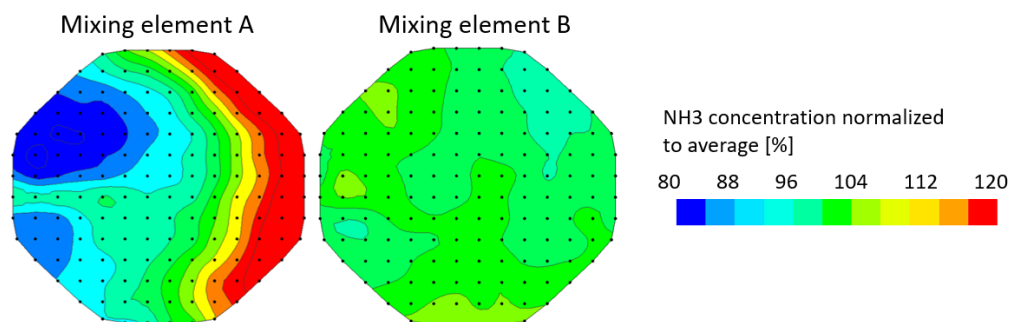
of the right spray cone, the surface temperatures agree well with 189.8 °C compared to 191.5 °C, yielding an error of only 1.7 °C.



**Figure 16.** Temperature–time diagram of the surface cooling at engine operating point 3 with injector 1 and resulting cooled areas in simulation and experiment after 50 s.

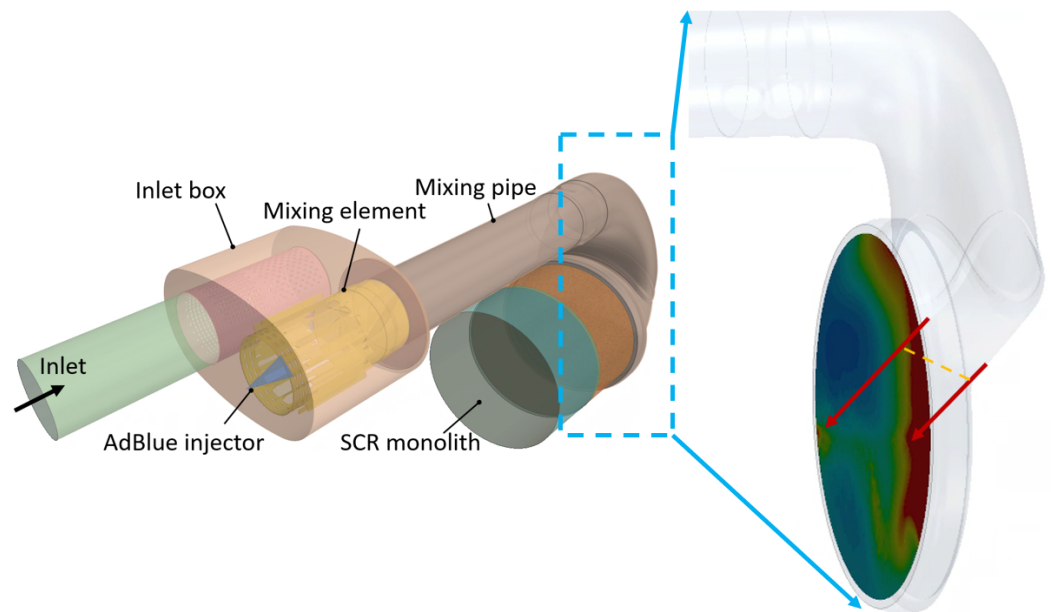
3.2. Validation Ammonia Uniformity

Figure 17 shows the measured ammonia distribution at the SCR catalyst outlet on the engine test bench. On the left, the result with only the swirl element (Figure 12: Mixer A) shows a UI of 93.8%. On the right, the excellent distribution with the additional mixing element (Figure 12: Mixer B) can be seen, yielding a UI of 98.9%.



**Figure 17.** Measured ammonia uniformity at the catalyst outlet on the engine test bench. **Left:** UI = 93.8%. **Right:** UI = 98.9%.

The measurement results for mixing element A show a horizontal line of average ammonia concentration (green) between the two lean areas (blue). It is caused by droplets sliding along the backside of the mixing pipe bend. They detach from the wall due to the pipe geometry, which acts like a trailing edge where the pipe opens towards the larger diameter catalyst housing after the bend, Figure 18. Superimposed on this effect, the gas flow in the inlet box encounters the spray from the side. The spray is pushed asymmetrically toward the right side of the mixing pipe. Then, following the swirling gas flow, the ammonia distribution is also not symmetrically on the catalyst inlet but shows a concentration increase from one side to another. In the case of geometry B, most droplets interact with the mixer blades before the flow can push them toward the side of the mixing pipe. Consequently, the asymmetry in the result is gone, and the uniformity improved.



**Figure 18.** The ammonia-rich horizontal line across the middle of the catalyst is caused by droplets sliding along the pipe wall before impacting and evaporating on the catalyst. The pipe’s opening towards the catalyst causes a trailing edge (dashed orange line) from where droplets separate (red arrows).

In Figure 19, the results of the CFD simulation with the presented impingement model are given. For variant A with swirl element, the ammonia distribution almost perfectly matches the measurement results in Figure 17. The high-concentration area on the right is captured correctly. The two lean regions on the left, with a more extensive and leaner upper section and a smaller, less intense lower area, are also well-replicated. The simulated UI of 93.6% is only 0.2%p off the measured value. The simulation result for variant B shows slight deviations from the measurements. An ammonia hot spot not seen on the test bench can be detected towards the left. Consequently, the UI of 97.4% is 1.5%p below the measurement results. Further analysis of the simulation results revealed that the hot spot is caused by UWS droplets impinging and evaporating on the catalyst inlet. The source of this ammonia-rich area is the same as described for the measurement results of mixing element A, with droplets sliding along the pipe wall before impacting the SCR brick, as depicted in Figure 18.

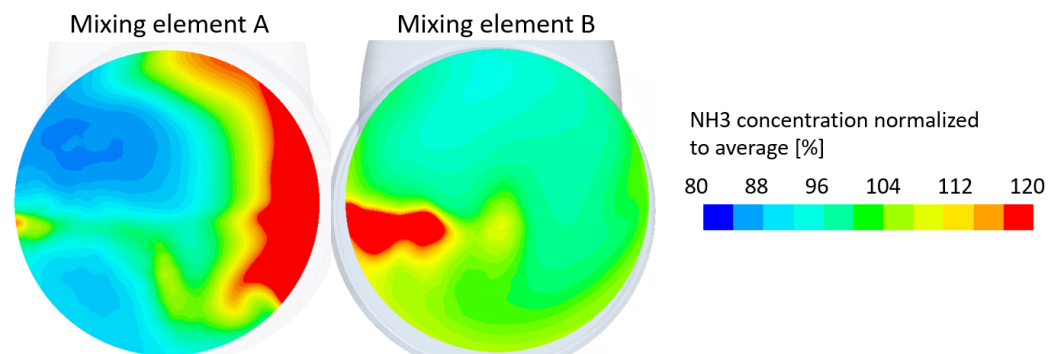


**Figure 19.** Simulated ammonia uniformity at the catalyst outlet. **Left:** UI = 93.6%. **Right:** UI = 97.4%.

It is assumed that the droplets slide along the pipe wall on a vapor cushion. While moving relative to the surface, the vapor cushion has to be built up constantly, causing ongoing evaporation. This effect could be enhanced by a curvature of the wall, as observed in a pipe bend, as it pushes the droplet against the wall. In the simulation, this droplet sliding consists of multiple individual impingement events to redirect the droplet path

constantly. As the impingement angle of these events is very flat, the wall-normal velocity of the repeated rebounds is minimal and yields very small *We*-numbers. While in reality the sliding is an ongoing contact, i.e., a very long contact time, the current model results in tiny values of contact time and area. Figure A1 shows that in the region of single-digit *We*-numbers, the observed contact area might be significantly larger than calculated for impingement angles of 22°. For near-wall-parallel droplet tracks, this effect could be even more substantial. Consequently, the evaporation of these sliding droplets in the simulation may be underestimated.

The underestimation of these droplets' evaporation can be seen for both geometries. For mixer A, a little area with overestimated ammonia concentration can be found on the left side of the horizontal center line. This area contributes to the reported minimal deviation in UI in this case. An ammonia hot spot can also be observed in the exact location for geometry B. However, mixer B pushes the droplets much stronger towards the pipe wall, causing more droplet mass to slide along the mixing pipe wall for a more considerable distance. In the measurement, this most likely causes complete evaporation of the droplet mass. Consequently, the described underestimation of this sliding evaporation in the simulation causes a more significant error for geometry B.

Although the result is not as excellent as for variant A, the differences between the two variants of mixing elements observed on the test bench are still captured to a large extent by the simulation results. The remaining deviation between the experiment and the simulation is most likely caused by the aforementioned sliding droplets. Here, further investigations with a specific focus might be needed to enable an extension of the model for this case.

The simulation results are improved by working on the heat transfer and the impingement outcome (regime classification and secondary droplet characteristics). To investigate the weighting of each effect on the overall results, simulations were carried out with the presented impingement model without evaporation from heat transfer. The results were very similar regarding the general ammonia distribution. Only the UI was decreased for both geometries by a few tenth-%p (mixer A: UI=93.1%, mixer B: UI=97.1%). The more significant improvement is, therefore, the impingement outcome modeling. For comparison, the results using a Bai–Gosman impingement model with best-practice settings [18] are shown in Appendix A.2, Figure A2. A significant improvement in accuracy with the new impingement model can be observed in the ammonia distribution and the resulting UI. The UI-deviations from the measurement results with the new model (0.2%p and 1.5%p) are significantly smaller than previously (6.9%p and 5.3%p).

#### 4. Conclusions

The article engages in modeling droplet–wall interaction. A particular focus is on the case of urea–water solution (UWS) droplets injected into the hot pipes of a selective catalytic reduction (SCR) system.

1. A new impingement model was presented based on superpositioned mass fractions of four basic impingement behaviors. Thus, the number of regimes can be reduced for simplification while the replication of observed transitional behavior is enabled. Measurements of secondary droplet characteristics were displayed and included in the model.
2. The heat transfer during droplet–wall interaction was implemented in the model following the approach presented in the literature by Wruck and adapted to the use with urea-water solution. This ensures that the effect of surface cooling from droplet–wall contact on the following impingement events is considered. For the model parameterization, additionally measured data of droplet–wall interaction were used.

The model was implemented in commercial CFD code Siemens Star-CCM+ v 17.02.008 for validation against measurement results:



3. The performance of the presented model in predicting the spray cooling behavior was shown on a flat impingement plate in the exhaust line of a diesel engine. The outline of the cooled-down areas could be simulated very well for different sprays and temperatures. The temperature–time diagrams also showed satisfactory agreement for multiple control areas. Especially the temperature-dependent change between fast- and slow-cooling impingement regimes could be replicated.
4. The potential of the impingement model to predict the ammonia distribution in a heavy-duty SCR aftertreatment system was illustrated. An almost perfect agreement between the experimental and the simulation results could be demonstrated for one geometry with a swirl element regarding ammonia distribution in the exhaust gas and uniformity index (UI). The simulation of a second mixer geometry showed slight deviations from the experimental results with an additional ammonia-rich area. Simulation analysis revealed droplets sliding along the hot pipe wall and then impinging on the catalyst as the source of the error. This effect of underestimated evaporation of sliding droplets is more significant with the additional mixing element B, which is the reason for the more substantial deviation from the experiments.

Applying the presented impingement model, a significant step forward in the simulation of droplet–wall interaction could be achieved. This is evidenced by the results of the validation cases. Nonetheless, the results also reveal possibilities for further improvement:

- i The particular case of sliding droplets on a hot wall seems to require further experimental investigations on a specific test bench setup and a derived modeling effort. Thus, slight remaining deviations between the simulation and experiment might be eliminated.
- ii The roughness influence on ammonia uniformity should be investigated, and a respective modeling approach presented in [11] assessed.
- iii An uncertainty regarding the effusivity of UWS in the highly transient case of droplet impingement was revealed in the current work. Appropriate experiments should be conducted to close this knowledge gap.

**Author Contributions:** Conceptualization, M.Q. and T.L.; Investigation, M.Q.; Data curation, M.Q. and S.P.; Funding acquisition, T.L.; Investigation, M.Q.; Methodology, M.Q. and U.B.; Validation, M.Q.; Formal analysis, M.Q.; Project administration, T.L.; Software, M.Q.; Supervision, T.L.; Writing—original draft, M.Q.; Writing—review and editing, M.Q. and T.L. All authors have read and agreed to the published version of the manuscript.

**Funding:** This work was funded by the Federal Ministry for Economic Affairs and Climate Action (BMWK) through the German Federation of Industrial Research Associations eV (AiF) based on a decision taken by the German Bundestag and the Research Association for Combustion Engines eV (FVV) (funding no. 601400). The work at the TU Wien was funded by the Ministry for Climate Action, Environment, Energy, Mobility, Innovation and Technology (BMK) through the Austrian Research Promotion Agency (FFG), grant number 877645. The research was carried out within the framework of the industrial collective programme (IGF/CORNET no. 270 EN). Open Access Funding by TU Wien.

**Data Availability Statement:** The data are not publicly available due to confidentiality reasons.

**Acknowledgments:** Special thanks to Melanie Walter for support with editing the diagrams.

**Conflicts of Interest:** The authors declare no conflicts of interest. The funders had no role in the design of the study; in the collection, analyses, or interpretation of data; in the writing of the manuscript; or in the decision to publish the results.

### Abbreviations

The following abbreviations are used in this manuscript:

CFD	Computational fluid dynamics
CHF	Critical heat flux
IR	Infrared
La	Laplace-number
LFP	Leidenfrost point
MBU	Mechanical breakup
MHF	Minimum heat flux
NO <sub>x</sub>	Nitric oxides
ONB	Onset of nucleate boiling
RANS	Reynolds averaged Navier Stokes
Re	Reynolds-number
SCR	Selective catalytic reduction
SMD	Sauter mean diameter
TBU	Thermal-induced breakup
$t_{inj}$	Injection duration
UI	Uniformity index
UWS	Urea-water solution
We	Weber-number
ZnSe	Zinc-selenide

### Appendix A

#### Appendix A.1. Contact Parameter Analysis

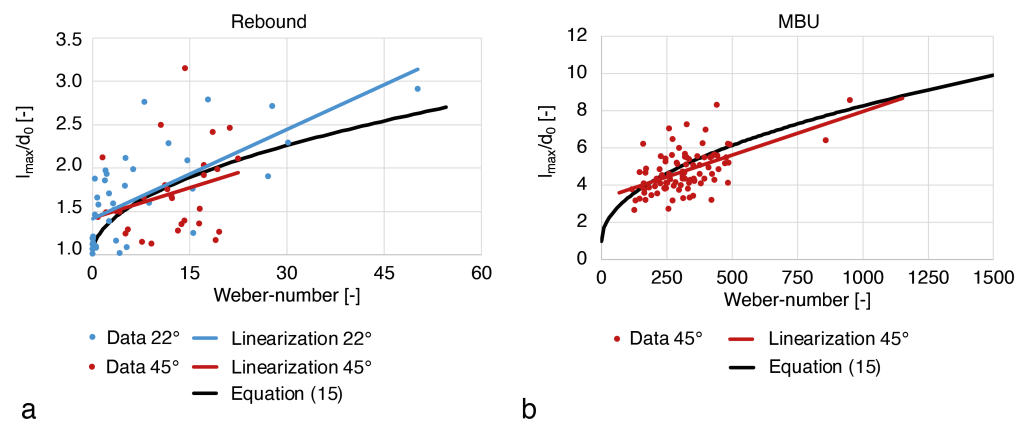


**Figure A1.** Measured ratio of contact patch length  $l_{max}$  to droplet diameter  $d_0$  over Weber-number for impingement data from 22° and 45° impingement angle and their linearization. As a reference, the function from Equation (15) [35] is added: (a) Rebound. (b) Mechanical breakup (MBU).

## Appendix A.2. Results Uniformity Modeling Best Practice Case

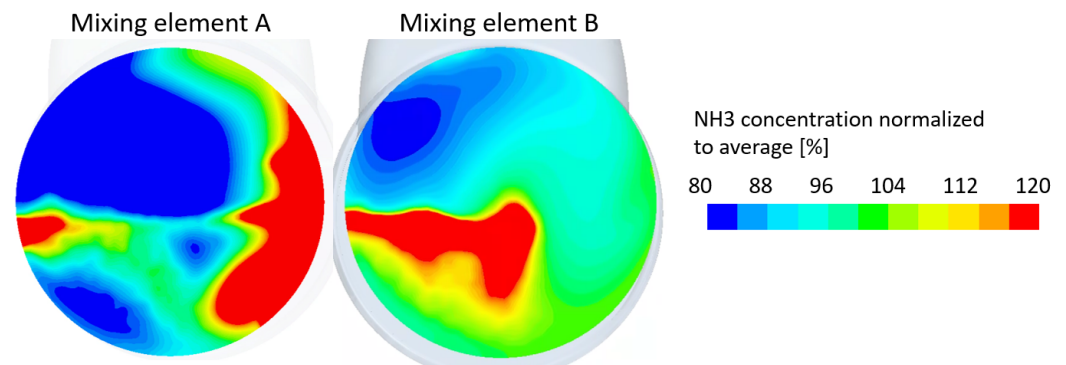


**Figure A2.** Simulated ammonia uniformity at the catalyst outlet with Bai–Gosman best-practice impingement model [18] without the additional implementation of a thermal-induced breakup. **Left:** UI = 86.9%. **Right:** UI = 93.6%.

## References

- Cravero, C.; de Domenico, D.; Marsano, D. The Use of Uncertainty Quantification and Numerical Optimization to Support the Design and Operation Management of Air-Staging Gas Recirculation Strategies in Glass Furnaces. *Fluids* **2023**, *8*, 76. [\[CrossRef\]](#)
- Birkhold, F. *Selektive katalytische Reduktion von Stickoxiden in Kraftfahrzeugen: Untersuchung der Einspritzung von Harnstoffwasserlösung*; Berichte aus der Strömungstechnik, Shaker: Aachen, Germany, 2007.
- Bai, C.; Gosman, A.D. Development of Methodology for Spray Impingement Simulation. *SAE Trans.* **1995**, *104*, 550–568.
- Kuhnke, D. Spray Wall Interaction Modelling by Dimensionless Data Analysis. Ph.D. Thesis, Technische Universität Darmstadt, Darmstadt, Germany, 2004.
- Wruck, N. *Transientes Sieden von Tropfen beim Wandaufprall*; Berichte aus der Verfahrenstechnik, Shaker: Aachen, Germany, 1999.
- Liang, G.; Mudawar, I. Review of drop impact on heated walls. *Int. J. Heat Mass Transf.* **2017**, *106*, 103–126. [\[CrossRef\]](#)
- Moita, A.S.; Moreira, A. Drop impacts onto cold and heated rigid surfaces: Morphological comparisons, disintegration limits and secondary atomization. *Int. J. Heat Fluid Flow* **2007**, *28*, 735–752. [\[CrossRef\]](#)
- Cossali, G.E.; Marengo, M.; Santini, M. Thermally induced secondary drop atomisation by single drop impact onto heated surfaces. *Int. J. Heat Fluid Flow* **2008**, *29*, 167–177. [\[CrossRef\]](#)
- Börnhorst, M.; Deutschmann, O. Single droplet impingement of urea water solution on a heated substrate. *Int. Heat Fluid Flow* **2018**, *69*, 55–61. [\[CrossRef\]](#)
- Kuhn, C.; Schweigert, D.; Kuntz, C.; Börnhorst, M. Single droplet impingement of urea water solution on heated porous surfaces. *Int. J. Heat Mass Transf.* **2021**, *181*, 121836. [\[CrossRef\]](#)
- Quissek, M.; Lauer, T. Impact of Surface Roughness on the Impingement of Urea–Water Solution Droplets. *Fluids* **2023**, *8*, 152. [\[CrossRef\]](#)
- Rioboo, R.; Tropea, C.; Marengo, M. Outcomes from a Drop Impact on Solid Surfaces. *At. Sprays* **2001**, *11*, 12. [\[CrossRef\]](#)
- Tran, T.; Staat, H.J.J.; Prosperetti, A.; Sun, C.; Lohse, D. Drop impact on superheated surfaces. *Phys. Rev. Lett.* **2012**, *108*, 036101. [\[CrossRef\]](#)
- Mundo, C.; Sommerfeld, M.; Tropea, C. Droplet-wall collisions: Experimental studies of the deformation and breakup process. *Int. J. Multiph. Flow* **1995**, *21*, 151–173. [\[CrossRef\]](#)
- Wachters, L.; Westerling, N. The heat transfer from a hot wall to impinging water drops in the spheroidal state. *Chem. Eng. Sci.* **1966**, *21*, 1047–1056. [\[CrossRef\]](#)
- Bai, C.X.; Rusche, H.; Gosman, A.D. Modeling of Gasoline Spray Impingement. *At. Sprays* **2002**, *12*, 1–28. [\[CrossRef\]](#)
- Smith, H.; Zöchbauer, M.; Lauer, T. *Advanced Spray Impingement Modelling for an Improved Prediction Accuracy of the Ammonia Homogenisation in SCR Systems*; SAE Technical Paper Series; SAE International: Warrendale, PA, USA, 2015. [\[CrossRef\]](#)
- Quissek, M.; Lauer, T.; García-Afonso, O.; Fowles, S. *Identification of Film Breakup for a Liquid Urea-Water-Solution and Application to CFD*; SAE Technical Paper Series; SAE International: Warrendale, PA, USA, 2019. [\[CrossRef\]](#)
- Quissek, M.; Budziankou, U.; Lauer, T. *A Novel Approach for the Impingement of AdBlue-Droplets based on Smooth Regime Transitions*; SAE Technical Paper Series; SAE International: Warrendale, PA, USA, 2020. [\[CrossRef\]](#)
- Mundo, C.; Tropea, C.; Sommerfeld, M. Numerical and experimental investigation of spray characteristics in the vicinity of a rigid Wall. *Exp. Therm. Fluid Sci.* **1997**, *15*, 228–237. [\[CrossRef\]](#)
- Gavaises, M.; Theodorakakos, A.; Bergeles, G. Modeling wall impactation of diesel sprays. *Int. J. Heat Fluid Flow* **1996**, *17*, 130–138. [\[CrossRef\]](#)
- Wang, D.M.; Watkins, A.P. Numerical modeling of diesel spray wall impactation phenomena. *Int. J. Heat Fluid Flow* **1993**, *14*, 301–312. [\[CrossRef\]](#)
- O'Rourke, P.J.; Amsden, A.A. A Spray/Wall Interaction Submodel for the KIVA-3 Wall Film Model. *J. Engines* **2000**, *109*, 281–298.

24. Nagaoka, M.; Kawazoe, H.; Nomura, N. Modeling Fuel Spray Impingement on a Hot Wall for Gasoline Engines. *J. Engines* **1994**, *103*, 878–896.
25. Naitoh, K.; Takagi, Y.; Kokita, H.; Kuwahara, K. Numerical Prediction of Fuel Secondary Atomization Behavior in SI Engine based on the Oval-Parabola Trajectories(OPT) Model. *J. Engines* **1994**, *103*, 897–914.
26. Naber, J.D.; Reitz, R.D. Modeling Engine Spray/Wall Impingement. *J. Engines* **1988**, *97*, 118–140.
27. Stanton, D.W.; Rutland, C.J. Multi-dimensional modeling of thin liquid films and spray-wall interactions resulting from impinging sprays. *Int. J. Heat Mass Transf.* **1998**, *41*, 3037–3054. [[CrossRef](#)]
28. Akao, F.; Araki, K.; Mori, S.; Moriyama, A. Deformation Behaviors of a Liquid Droplet Impinging onto Hot Metal Surface. *Trans. Iron Steel Inst. Jpn.* **1980**, *20*, 737–743. [[CrossRef](#)]
29. Naber, J.D.; Farrell, P.V. Hydrodynamics of Droplet Impingement on a Heated Surface. *J. Engines* **1993**, *102*, 1346–1361.
30. Senda, J.; Kobayashi, M.; Iwashita, S.; Fujimoto, H. Modeling of Diesel Spray Impingement on a Flat Wall. *J. Engines* **1994**, *103*, 1918–1931.
31. Bernardin, J.D.; Stebbins, C.J.; Mudawar, I. Effects of surface roughness on a water droplet impact history and heat transfer regimes. *Int. J. Heat Mass Transf.* **1997**, *40*, 73–88. [[CrossRef](#)]
32. Koizumi, Y. Outline of Boiling Phenomena and Heat Transfer Characteristics. In *Boiling*; Elsevier: Amsterdam, The Netherlands, 2017; pp. 1–11. [[CrossRef](#)]
33. Budziankou, U.; Lauer, T.; Yu, X.; Schmidt, B.M.; Cho, N. *Modeling Approach for a Wiremesh Substrate in CFD Simulation*; SAE Technical Paper Series; SAE International: Warrendale, PA, USA, 2017. [[CrossRef](#)]
34. Budziankou, U.; Lauer, T. Modeling of Deposit Formation in SCR-Systems. Doctoral thesis, Technische Universität Wien, Wien, Austria, 24 March 2022.
35. Castanet, G.; Caballina, O.; Lemoine, F. Drop spreading at the impact in the Leidenfrost boiling. *Phys. Fluids* **2015**, *27*, 063302. [[CrossRef](#)]
36. Karl, A.; Anders, K.; Rieber, M.; Frohn, A. Deformation of liquid droplets during collisions with hot walls: Experimental and Numerical Results. *Part. Part. Syst. Charact.* **1996**, *13*, 186–191. [[CrossRef](#)]
37. Ueda, T.; Enomoto, T.; Kanetsuki, M. Heat Transfer Characteristics and Dynamic Behavior of Saturated Droplets Impinging on a Heated Vertical Surface. *Bull. JSME* **1979**, *22*, 724–732. [[CrossRef](#)]
38. Bianco, A.L.; Chevy, F.; Clanet, C.; Lagubeau, G.; Quéré, D. On the elasticity of an inertial liquid shock. *J. Fluid Mech.* **2006**, *554*, 47. [[CrossRef](#)]
39. Karl, A.; Frohn, A. Experimental investigation of interaction processes between droplets and hot walls. *Phys. Fluids* **2000**, *12*, 785–796. [[CrossRef](#)]
40. Akhtar, S.W.; Yule, A.J. Droplet Impaction on a Heated Surface at High Weber Numbers. In Proceedings of the 17th ILASS-Europe, Zurich, Switzerland, 2–6 September 2001.
41. Budziankou, U.; Quissek, M.; Lauer, T. Deposit Formation in SCR-Systems - Optical Investigations. *SAE Int. J. Adv. Curr. Pract. Mobil.* **2021**, *3*, 501–515. [[CrossRef](#)]
42. Budziankou, U.; Quissek, M.; Lauer, T. *A Fast Modeling Approach for the Numerical Prediction of Urea Deposit Formation*; SAE Technical Paper Series; SAE International: Warrendale, PA, USA, 2020. [[CrossRef](#)]
43. Börnhorst, M.; Budziankou, U.; Deutschmann, O.; Lauer, T. *Fundamental Experimental and Numerical Investigations on the Deposit Formation and Decomposition from AdBlue in SCR-Systems*; FVV Final Project Report 1262; FVV: Frankfurt am Main, Germany, 2019.
44. Fischer, S. Simulation of the Urea-Water-Solution Preparation and Ammonia-Homogenization with a Validated CFD-Model for the Optimization of Automotive SCR-Systems. Ph.D. Thesis, Technische Universität Wien, Wien, Austria, 2012.
45. Davidson, L.; Nielsen, P.; Sveringsson, A. Modifications of the V2 Model for Computing the Flow in a 3D Wall Jet. In Proceedings of the Proceedings of the International Symposium on Turbulence, Heat and Mass Transfer, Antalya, Turkey, 12–17 October 2003.
46. Siemens. Simcenter STAR-CCM+ User Guide. 2022. Available online: [https://docs.sw.siemens.com/en-US/doc/226870983/PL2\\_0220315376513299.starccmp\\_userguide\\_html?audience=external](https://docs.sw.siemens.com/en-US/doc/226870983/PL2_0220315376513299.starccmp_userguide_html?audience=external) (accessed on 7 June 2023).
47. Zöchbauer, M.; Fischer, S.; Lauer, T.; Siegmund-Hegerfeld, T.; Harasek, M.; Krenn, C.; Pessl, G. *Validation of Turbulence Models for an Automotive SCR System with Laser Doppler Anemometry Measurements*; SAE Technical Paper Series; SAE International: Warrendale, PA, USA, 2013. [[CrossRef](#)]
48. Lardeau, S.; Billard, F. Development of an elliptic-blending lag model for industrial applications. In Proceedings of the 54th AIAA Aerospace Sciences Meeting, San Diego, CA, USA, 4–8 January 2016; American Institute of Aeronautics and Astronautics: Reston, VA, USA, 2016. [[CrossRef](#)]

**Disclaimer/Publisher’s Note:** The statements, opinions and data contained in all publications are solely those of the individual author(s) and contributor(s) and not of MDPI and/or the editor(s). MDPI and/or the editor(s) disclaim responsibility for any injury to people or property resulting from any ideas, methods, instructions or products referred to in the content.